**PAPER**

# Total variation regularization in measurement and image space for PET reconstruction

View the article online for updates and enhancements.

# Total variation regularization in measurement and image space for PET reconstruction

## M Burger[1], J Müller[2], E Papoutsellis[3] and C B Schönlieb[3]

[1] Institute for Computational Applied Mathematics and Cells-in-Motion Cluster of Excellence (EXC 1003 CiM), University of Münster, Germany
[2] Department of Nuclear Medicine, University Hospital Münster, Germany
[3] Department of Applied Mathematics and Theoretical Physics, University of Cambridge, UK

E-mail: martin.burger@wwu.de, jahn.mueller@uni-muenster.de, ep374@cam.ac.uk and cbs31@cam.ac.uk

## Abstract

The aim of this paper is to test and analyse a novel technique for image reconstruction in positron emission tomography, which is based on (total variation) regularization on both the image space and the projection space. We formulate our variational problem considering both total variation penalty terms on the image and on an idealized sinogram to be reconstructed from a given Poisson distributed noisy sinogram. We prove existence, uniqueness and stability results for the proposed model and provide some analytical insight into the structures favoured by joint regularization. For the numerical solution of the corresponding discretized problem we employ the split Bregman algorithm and extensively test the approach in comparison to standard total variation regularization on the image. The numerical results show that an additional penalty on the sinogram performs better on reconstructing images with thin structures.

Keywords: variational regularization, positron emission tomography, total variation

(Some figures may appear in colour only in the online journal)

## 1. Introduction

Positron emission tomography (PET) is a medical imaging technique for studying functional characteristics of the human body, used in brain imaging, neurology, oncology and recently also in cardiology. The patient is injected with a dose of radioactive tracer isotope which concentrates in tissues of interest in the body. Typically, cells in the tissue which are more active have a higher metabolism, i.e., need more energy, and hence will absorb more tracer isotope than cells which are less active. The isotope suffers radioactive decay which invokes it to emit a positron. As soon as the emitted positron meets an electron a pair of gamma rays is sent out into approximately opposite directions and is picked up by the PET-scanner. The collection of all these pairs builds the PET measurement *g* from which the distribution *u* of the relevant radiopharmaceutical shall be reconstructed.

As a (yet simplified) mathematical model the PET measurement can be interpreted as a sample of

$$f = e^{-\int_L h \, dt} \int_L u \, dt, \tag{1.1}$$

where the above integral is the Radon transform $\mathcal{R}$ of *u* along the line *L* connecting the emission point of the gamma rays and the detector, see figure 1; the above exponential characterizes the damping due to the 'attenuation' function *h* (which is, e.g., known from CT [36 chapter 7]). The function *f(L)* is called the sinogram of *u*. Since the attenuation can be corrected beforehand we shall ignore the attenuation term in the solution of the inverse problem (corresponding to $h \equiv 0$) in this paper. The basic mathematical problem for the reconstruction of the distribution *u*, is the inversion of the Radon transform. In PET, this inversion is complicated by the presence of undersampling and noise [36]. The PET data usually is corrupted by Poisson noise, also called photon noise, due to the photon counting process during the PET scan.

In this paper, we propose a novel technique for reconstructing an image *u* from noisy PET measurements *g* by a variational regularization approach using total variation (TV) regularization [28] on both the image *u* and the sinogram $\mathcal{R}u$. More precisely, let $\Sigma^n = \{(\theta, s) \in S^{n-1} \times \mathbb{R}\}$ be the projection space (see figure 1) and $\mathbb{R}^2$ the physical space. The Radon transform $\mathcal{R}: L^1(\mathbb{R}^2) \to L^1(\Sigma)$ of $u \in L^1(\mathbb{R}^2)$ is given by

$$\mathcal{R}u(\theta, s) = \int_{\mathbb{R}^2} u(x)\delta(s - x \cdot \theta)dx. \tag{1.2}$$

Given measurements $g \in L^2(\Sigma)$, we reconstruct $u \in BV(\mathbb{R}^2)$ by solving

$$\underset{u \in BV(\mathbb{R}^2), \, u \geqslant 0 \text{ a.e. in } \mathbb{R}^2}{\arg\min} \left\{ \alpha \, |Du|(\mathbb{R}^2) + \beta \, |D(\mathcal{R}u)|(\Sigma) + \frac{1}{2} \int_\Sigma \frac{(g - \mathcal{R}u)^2}{g} \right\}. \tag{1.3}$$

Here $BV(\mathbb{R}^2)$ is the space of functions of bounded variation, see [2], and $\alpha$, $\beta$ are positive parameters. The terms $|Du|(\mathbb{R}^2)$ and $|D(\mathcal{R}u)|(\Sigma)$ are TV regularizations on the image *u* and the sinogram $\mathcal{R}u$ respectively, that is

$$|Du|\left(\mathbb{R}^2\right) = \sup_{\mathbf{g} \in C_0^\infty\left(\mathbb{R}^2; \mathbb{R}^2\right), \|g\|_\infty \leqslant 1} \int_{\mathbb{R}^2} u \, \nabla \cdot \mathbf{g} \, dx,$$

$$|D\mathcal{R}u|\left(\Sigma\right) = \sup_{\mathbf{g} \in C_0^\infty\left(\Sigma; \mathbb{R}^2\right), \|g\|_\infty \leqslant 1} \int_\Sigma \mathcal{R}u \, \nabla \cdot \mathbf{g} \, dx.$$
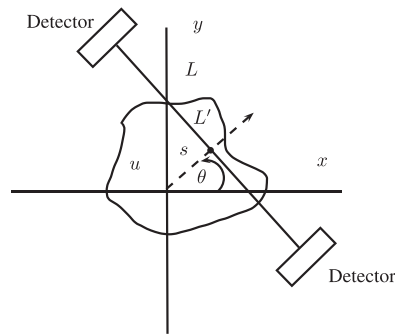
**Figure 1.** PET scan geometry. The image function $u$ is encoded in integrals $f(L) = f(\theta, s)$ along lines $L$ from the emission point to the detectors, see (1.1). The lines $L$ are defined by an angle $\theta$ and distance $s$ to the origin. ($L'$ is the distance from the emission point through the object).

The data fidelity $\int_{\Sigma} (g - \mathcal{R}u)^2 / g$ is a weighted $L^2$ norm that constitutes a standard approximation of the Poisson noise model given by the Kullback–Leibler divergence, compare [29, chapter 4] for instance.

PET reconstruction using TV regularization is not new. However, typically the TV regularization is applied to the image function $u$ only. By additionally regularizing the sinogram $\mathcal{R}u$ using a total variation penalty in projection space we will show that under certain conditions images of higher quality can be reconstructed. In particular, this is the case in the presence of high noise in $g$ and when aiming to preserve thin and elongated structures in $u$.

## 1.1. Related methods

Our approach (1.3) is inspired by an alternating regularization procedure for PET first introduced by Barbano et al. in [3]. Given possible under sampled and noisy PET measurements $g \in \mathbb{R}^{n \times m}$ an image $u^*$ is reconstructed by solving

$$\min_{\{(s,u) : \, s \in \mathbb{R}^{n \times m}, u = \mathcal{R}^{-1}s\}} \alpha \, \| \nabla s \|_1 + \beta \, \| u \|_1 + \frac{\lambda}{2} \, \| g - s \|_2^2, \tag{1.4}$$

where $\mathcal{R}^{-1}$ is the inverse Radon transform approximated by the filtered backprojection and $\alpha$, $\beta$ and $\lambda$ are positive weighting parameters. Note that here a regularized reconstruction $u^*$ is computed by smoothing both the image $u$ and the sinogram $s$. Indeed, the regularization in (1.4) is given by the total variation regularizer $\| \nabla s \|_1$, see [28], that acts on the sinogram $s$ only. The image $u$ is forced to be sparse by an $\ell_1$ penalty. The main focus of [3] is to study the effect of total variation regularization on the sinogram, rather than the image as usually done in variational PET reconstruction [10, 11, 30, 31]. Therefore, in their numerical experiment the effect of the image regularization is kept low by choosing an appropriate weighting $\alpha \gg \beta$. In [3] it is proved that (1.4) has a unique solution $(s^*, u^*)$. Moreover, the authors show the effect, the total variation regularization of the sinogram $s$, has on the reconstructed image $u$ by a computational experiment on a simulated data set.

The main idea of adding a total variation regularization on the projection space originated in the works of Thirion [34], and Prince *et al* [27]. In [34] the author proposes to connect edge detection of the tomographic image to finding continuous lines in the sinogram. That is, a point on a line in the sinogram corresponds to an edge in the object space with a fixed

orientation and distance from the origin, see figure 1. Moreover, in [27] Prince and Willsky focus on reconstructing tomographic images by using a Markov random field prior on the sinogram, in particular in the presence of data with a low signal-to-noise ratio (SNR) and limited angle or sparse-angle measurement configurations. Their approach leads to the computation of a smoothed sinogram from which the image $u$ is reconstructed using filtered back projection.

## 1.2. State of the art—direct and iterative PET reconstruction

In (1.3) we reconstruct an image from PET measurements by smoothing both in measurement and image space. This indeed combines the philosophies of the two main approaches for image reconstruction from PET measurements: (i) direct methods and (ii) iterative variational method. While in direct methods the PET measurements are smoothed by an appropriate filter and then inverted (see e.g. [22, 24]), iterative methods (respectively variational methods solved iteratively) are based on the standard Bayesian modelling approach in inverse problems in which prior knowledge in terms of regularity is expressed for the image function $u$ (rather than the measurements $f$). The possibility to include statistical noise models is a main advantage of iterative and variational methods, on which we shall focus in the following.

In iterative methods for PET reconstruction the noise distribution is accounted for by modelling the randomness in the numbers of detected gamma counts. The most popular iterative approach for PET reconstruction is the expectation-maximization (EM) algorithm. To recall, the problem of image reconstruction can be formulated as a solution of the linear and ill-conditioned operator equation:

$$g = Ku,$$

where $g$ is the Poisson distributed data and $K$ is a finite-dimensional sampling of the Radon transform. Typically, we may assume that the data are realizations of random variables $X_i$ and we consider the detected values $g_i$ as a realization of a random variable $X_i$, for $i = 1,...,N$. It is reasonable to maximize the conditional probability $P(u \mid g)$, which by the Bayes' Law is:

$$P(u \mid g) = \frac{P(g \mid u)P(u)}{P(g)}.$$

It is equivalent to maximize $P(g \mid u)P(u)$, since the denominator does not depend on $u$. Moreover, the random variables of the measured data are Poisson distributed with expected values given by $(Ku)_i$ and

$$P(g \mid u) = \prod_{i=1}^{N} \frac{(Ku)_i^{g_i}}{g_i!} e^{-(Ku)_i}. \tag{1.5}$$

The Bayesian approach allows to consider additional information to our model with an appropriate prior probability of the image $u$, see [15, 21]. The most frequently used prior densities are the Gibbs priors, i.e.,

$$P(u) = e^{-\alpha J(u)}, \tag{1.6}$$

where $\alpha > 0$ is a regularization parameter and $J(u)$ is a convex energy functional. Instead of maximizing $P(g \mid u)P(u)$, we minimize $-\log(P(g \mid u)P(u))$. Hence, we seek a minimizer of the following problem

$$\arg\min_{u \geq 0} \left\{ \sum_{i=1}^{N} \left( (Ku)_i - g_i \log (Ku)_i \right) + \alpha J(u) \right\}, \tag{1.7}$$

where the first term is the so-called Kullback–Leibler divergence of $u$ and $g$. This often serves as a motivation to consider the continuous variational problem

$$\arg\min_{u \geq 0} \left\{ \int (Ku - g \log (Ku)) + \alpha J(u) \right\}. \tag{1.8}$$

In the case where $J \equiv 0$, the first optimality condition in (1.8) yields the following iterative scheme, known as EM algorithm

$$u^{k+1} = \frac{u^k}{K^*1} K^* \left( \frac{g}{Ku_k} \right).$$

Additionally imposing prior information on the solution, e.g., that the solutions has a small total variation, leads to an extension of the EM algorithm, e.g., the EM-TV algorithm [4, 10]. See also [5, 30, 31, 37] for related approaches and [10, 11] for extensions of EM-TV to Bregmanized total variation regularization.

*Outline*

The rest of the paper is organized as follows: in the next section we prove existence, uniqueness and stability results for our variational model in the continuous setting. In section 3, we focus on solving numerically our problem using the split Bregman method and present our numerical simulations in section 4.

## 2. TV regularization on image and sinogram

In this section, we will discuss the well-posedness of our minimization problem (1.3). To do so, we first rewrite (1.3) for image functions $u$ that are defined on a bounded and open domain $\Omega \subset \mathbb{R}^2$ including sufficiently large balls around zero. We consider the following problem

$$\arg\min_{u \in BV(\Omega),\ u \geq 0 \text{ a.e. in } \Omega} \left\{ F(u) = \ \alpha\, |Du|(\Omega) + \beta\, |D(\mathcal{R}u)|(\Sigma) \right.$$
$$\left. + \frac{1}{2} \int_{\Sigma} \frac{(g - \mathcal{R}u)^2}{g} \right\}. \tag{2.1}$$

We enforce prior information in terms of regularization on both the image and its sinogram. Note, that the TV regularization on the sinogram in (2.1) has a different effect on the reconstructed image compared to regularizing in image space ($\beta = 0$) only. Of course, regularization of the image $u$ enforces a certain regularization of the sinogram $\mathcal{R}u$ as well. However, because of the nonlinear character of the total variation regularization, TV regularization of the sinogram is not equivalent to regularization on the image and vice-versa. In (2.1) the two types of TV regularization impose different structures in the subgradients of the two terms. This is also emphasized in section 2.4 where the source condition (2.22) and the elements $p_1$, $p_2$ are described. Indeed, beyond the topology imposed by the regularizer the structure imposed by the sub gradients of the total variation regularizers are crucial for the properties of a solution of (2.1). In particular, in what follows we will see that the additional TV regularization on the sinogram can have a positive effect when reconstructing smooth, thin structures as can be observed in the myocardium for instance. This effect will be both

motivated analytically by the characterization of a solution of (2.1) for the simple case when $g$ is the sinogram of a disc for instance, as well as experimentally verified by testing the method against some representative examples in the numerical part of the paper.

We start with some first observations that are crucial ingredients of the well-posedness analysis for (2.1). In order not to divide by zero in the weighted $L^2$ norm in (2.1), we first assume that there exists constant $c_1 > 0$ such that

$$0 < c_1 \leqslant g(\theta, s) \leqslant \| g \|_{L^\infty(\Sigma)}. \tag{2.2}$$

The constraint (2.2) is not significantly restrictive in most medical experiments. Since $u$ is assumed to be non-negative, this basically can be achieved if the lines in the Radon transform are confined to those intersecting the support of $u$, at least in a discretized setting.

Moreover, to justify the definition of $F(u)$ in (2.1) over the admissible set $\{u \in BV(\Omega), u \geqslant 0 \text{ a.e. in } \Omega\}$ in theorem 2.1 we show that the Radon transform of $u$ is again in $BV$. To do so it is important to assume that the object we wish to recover is compactly supported. Hence, we may assume that $\operatorname{supp} u \subset B_r \subset \Omega$, where $B_r$ is the ball with radius r centered at the origin. Consequently, (1.2) implies that $\mathcal{R}u(\theta, s) = 0$, when $s \notin [-r, r]$ and the projection space becomes:

$$\Sigma = \{(\theta, s): -r \leqslant s \leqslant r, 0 \leqslant \theta < \pi\}. \tag{2.3}$$

If it is not stated otherwise, we will always assume that the reconstructed image is compactly supported. Note that, we allow negative values on the s variable and that we do not consider the Radon transform for $\theta = \pi$. Likewise, we may allow that $s \geqslant 0$ and $0 \leqslant \theta < 2\pi$. Hence, we consider the Radon space $\Sigma$ as the surface of a half cylinder with radius 1. Moreover, since Dirac $\delta$ function is even, equation (1.2) implies that the coordinates $(-s, \phi)$ and $(s, \phi + \pi)$ correspond to the same point in the Radon space.

### 2.1. BV-continuity of the Radon transform

Our first result deals with a continuity property for the Radon transform as a mapping operator for functions with bounded variation. A similar result is proved by M Bergounioux and E Trélat [8] in the three dimensional case and for bounded and axially symmetric objects.

In what follows we do not need this symmetry assumption, but prove that the Radon transform is BV continuous for compactly supported $u$ in two space dimensions.

**Theorem 2.1.** *Let $u \in BV(\Omega)$ and the ball $B_r$ with radius r be its compact support, then $\mathcal{R}u \in BV(\Sigma)$ and the Radon transform is BV continuous on the subspace of functions supported in $B_r$.*

**Proof.** It is well known that the Radon transform is $L^1$ continuous and the following estimate holds for $n \geqslant 2$:

$$\| \mathcal{R}u \|_{L^1(\Sigma^n)} \leqslant \left| S^{n-1} \right| \| u \|_{L^1(\mathbb{R}^n)}. \tag{2.4}$$

Hence, to prove BV-continuity we need to prove that the variation of $\mathcal{R}u$ over $\Sigma$ is finite and bounded by the BV norm of $u$, i.e.,

$$V(\mathcal{R}u, \Sigma) = \sup \left\{ \int_\Omega \mathcal{R}u(\theta, s) \operatorname{div} g(\theta, s) \mathrm{d}\theta \mathrm{d}s: \ g \in \left( C_c^1(\Sigma) \right)^2, \| g \|_\infty \leqslant 1 \right\} < \infty.$$

The following equations can easily be derived by the geometry depicted in figure 1, where $(x, y)$ is the annihilation point and $t$ runs through the line $L$:

$$x = s \cos \theta - t \sin \theta, \qquad (2.5)$$

$$y = s \sin \theta + t \cos \theta. \qquad (2.6)$$

We may also assume that $t \in [-r, r]$. Therefore,

$$\int_{\Omega} \mathcal{R} u(\theta, s) \operatorname{div} g(\theta, s) \mathrm{d}\theta \mathrm{d}s = \underset{\operatorname{div} g(\theta, s) \, \mathrm{d}t\mathrm{d}s\mathrm{d}\theta}{\int_0^\pi \int_{-r}^r \int_{-r}^r} u(s \cos \theta - t \sin \theta, s \sin \theta + t \cos \theta)$$

$$= \int_0^\pi \int_{-r}^r \int_{-r}^r u(x, y) \Big[ \nabla g_1 \cdot \vec{\alpha}$$

$$+ \nabla g_2 \cdot \vec{\theta} \Big] \mathrm{d}x\mathrm{d}y\mathrm{d}\theta,$$

where $\vec{\alpha} = (-y, x), \vec{\theta} = (\cos \theta, \sin \theta)$ and in the above calculations we have used (2.5)(2.6). Define, $\vec{G}(x, y) = (G_1(x, y), G_2(x, y))$ with

$$G_1(x, y) = \int_0^\pi - y g_1(\theta, x \cos \theta + y \sin \theta) + g_2(\theta, x \cos \theta + y \sin \theta) \cos \theta \mathrm{d}\theta$$

$$G_2(x, y) = \int_0^\pi x g_1(\theta, x \cos \theta + y \sin \theta) + g_2(\theta, x \cos \theta + y \sin \theta) \sin \theta \mathrm{d}\theta$$

then,

$$\operatorname{div} G(x, y) = \frac{\partial g_1}{\partial x} + \frac{\partial g_2}{\partial y} = \int_0^\pi \left( \nabla g_1 \cdot \vec{\alpha} + \nabla g_2 \cdot \vec{\theta} \right) \mathrm{d}\theta.$$

The function $G$ lies in $C^1(\mathbb{R}^2)$ and if we restrict $G$ on $\Omega$ and consider $G\chi_{B_r}$ then $G \in C_c^1(\Omega)$. Moreover,

$$\big| G_1(x, y) \big| \leqslant \int_0^\pi |y| \big| g_1 \big| + \big| g_2 \big| \leqslant \pi \| g \|_\infty (1 + |y|) \leqslant \pi \| g \|_\infty (1 + r) = C$$

and $|G_2(x, y)| \leqslant C$. If we set

$$A = \int_{-r}^r \int_{-r}^r u(x, y) \operatorname{div} G(x, y) \mathrm{d}x\mathrm{d}y = C \int_{-r}^r \int_{-r}^r u(x, y) \operatorname{div} \left( \frac{G(x, y)}{C} \right) \mathrm{d}x\mathrm{d}y$$

and

$$B = \int_{\Sigma} \mathcal{R} u(\theta, s) \operatorname{div} g(\theta, s) \mathrm{d}s\mathrm{d}\theta$$

then, taking the supremum over all $G \in C_c^1(\Omega)$ with $\| G/C \|_\infty \leqslant 1$, we have that $B = C \cdot V(u, \Omega)$. Similarly, for all $g \in \left( C_c^1(\Sigma) \right)^2$ with $\| g \|_\infty \leqslant 1$, we conclude that

$$V(\mathcal{R} u, \Sigma) \leqslant \pi(1 + r) V(u, \Omega) < \infty.$$

Therefore, $\mathcal{R} u \in BV(\Sigma)$ and the variation coincides with the total variation $|D(\mathcal{R} u)|(\Sigma)$. By the corresponding norm defined on the BV space and equation (2.4), we deduce that

$$\| \mathcal{R} u \|_{BV(\Sigma)} \leqslant \pi(1 + r) \| u \|_{BV(\Omega)}.$$

$\square$

## 2.2. Existence and uniqueness

Next, we show existence and uniqueness of the minimizer for the problem (2.1).

**Theorem 2.2.** *Let $\alpha > 0$, $\beta \geqslant 0$ and $g \in L^\infty(\Sigma)$ a strictly positive function. Then the functional $F(u)$ in (2.1) is lower semicontinuous and strictly convex and the minimization problem (2.1) attains a unique solution $u \in BV(\Omega) \cap L^1_+(\Omega)$.*

**Proof.** Let $(u_n)_n \in BV(\Omega)$ be a minimizing sequence of non-negative functions, then in particular there exists a constant $C_1 > 0$ such that

$$F(u) = \alpha \left| Du_n \right| (\Omega) + \beta \left| D\left( \mathcal{R}u_n \right) \right| (\Sigma) + \frac{1}{2} \int_\Sigma \frac{\left( g - \mathcal{R}u_n \right)^2}{g} < C_1. \quad (2.7)$$

Let $\overline{u}_n = \frac{1}{|\Omega|} \int_\Omega u_n \mathrm{d}x$, then by the Poincaré–Wirtinger inequality [2], we can find a constant $C_2 > 0$ such that

$$\left\| u_n - \overline{u}_n \right\|_{L^2(\Omega)} \leqslant C_2 \left| Du_n \right| (\Omega). \quad (2.8)$$

Therefore

$$\left\| u_n \right\|_{L^2(\Omega)} \leqslant C_2 \left| Du_n \right| (\Omega) + \left| \int_\Omega u_n \mathrm{d}x \right|.$$

Following the proof of [35], we set $v_n = u_n - \overline{u}_n$ and since

$$C_1 \geqslant \int_\Sigma \frac{\left( g - \mathcal{R}u_n \right)^2}{g} \geqslant \frac{1}{\| g \|_{L^\infty(\Sigma)}} \left\| g - \mathcal{R}u_n \right\|^2_{L^2(\Sigma)}$$

one can prove that

$$\begin{aligned}
\left\| \mathcal{R}\overline{u}_n \right\|_{L^2(\Sigma)} &\leqslant C_1 \| g \|_{L^\infty(\Sigma)} + \left\| \mathcal{R}v_n \right\|_{L^2(\Sigma)} + \| g \|_{L^2(\Sigma)} \\
&\leqslant \widetilde{C}_1 \| g \|_{L^\infty(\Sigma)} + \left\| \mathcal{R}v_n \right\|_{L^2(\Sigma)}
\end{aligned}$$

and

$$\left| \frac{1}{|\Omega|} \int_\Omega u_n \mathrm{d}x \right| \cdot \left\| \mathcal{R}\chi_\Omega \right\|_{L^2(\Sigma)} = \left\| \mathcal{R}\overline{u}_n \right\|_{L^2(\Sigma)}.$$

Without loss of generality, we may assume that the image domain $\Omega$ is a unit square, then $\mathcal{R}\chi_\Omega \neq 0$, see [26, chapter 8] and we conclude that $| \int_\Omega u_n dx |$ is uniformly bounded. Hence, $u_n$ is $L^1(\Omega)$ bounded ($L^2(\Omega)$ bounded with $|\Omega| < \infty$). Moreover, since the Radon transform is $L^2$ continuous for functions with compact support (see [20, 24]) and using (2.4), we have the following:

Since, $(u_n)_{n \in \mathbb{N}}$ is bounded in $L^1(\Omega)$ and $|Du_n|(\Omega) < \infty$ i.e., is $BV(\Omega)$ bounded, we obtain a subsequence $(u_{n_k})_{k \in \mathbb{N}}$, $u \in BV(\Omega)$ such that $u_{n_k}$ converges weakly* to u. Also, $u_{n_k}$ converges weakly to u in $L^2(\Omega)$. Then,

$$\mathcal{R}u_{n_k} \to \mathcal{R}u \text{ in } L^1(\Sigma) \quad (2.9)$$

$$\mathcal{R}u_{n_k} \rightharpoonup \mathcal{R}u \text{ in } L^2(\Sigma). \quad (2.10)$$

Then,

$$|D(\mathcal{R}u)|(\Sigma) \leqslant \liminf_{k \to \infty} \left| D\left( \mathcal{R}u_{n_k} \right) \right| (\Sigma)$$

and the weak lower semicontinuity of the $L^2$ norm and the lower semicontinuity of total variation semi-norm for both the image and the projection space imply that

$$F(u) \leqslant \liminf_{k \to \infty} F(u_{n_k}).$$

To prove uniqueness let $0 \leqslant u_1, u_2 \in BV(\Omega)$ be two minimizers. If $\mathcal{R}u_1 \neq \mathcal{R}u_2$, then the strict convexity of the weighted $L^2$ fidelity term together with the convexity of the total variation of $\mathcal{R}u$ implies that:

$$F\left(\frac{u_1 + u_2}{2}\right) < \frac{F(u_1)}{2} + \frac{F(u_2)}{2} = \inf_{\substack{u \in BV(\Omega) \\ u \geqslant 0 \text{ a.e.}}} F(u)$$

which is a contradiction. Hence, $\mathcal{R}u_1 = \mathcal{R}u_2$ and using the well-known *Slice-Projection* theorem i.e.,

$$\mathcal{F}\left(\mathcal{R}_\theta u(s)\right) = (2\pi)^{\frac{n-1}{2}} \mathcal{F}_n(u(s\theta)),$$

where the right-hand side denotes the n-dimensional Fourier transform, we conclude that $u_1 = u_2$, see also [23, 24] for more details. $\qquad\square$

### 2.3. Stability

Further, we discuss the stability of problem (2.1) in terms of a small perturbation on the data. Following the approach of Acar and Vogel in [1], we consider a perturbation on the projection space i.e.,

$$g_n = g + \tau_n \text{ with } \left\|\tau_n\right\|_{L^2(\Sigma)} \to 0 \tag{2.11}$$

and define the corresponding minimization problem on the perturbed functionals:

$$\underset{u \geqslant 0 \text{ a.e}, u \in BV(\Omega)}{\arg\min} \left\{ F^n(u) = \alpha\,|Du|(\Omega) + \beta\,|D(\mathcal{R}u)|(\Sigma) \right.$$

$$\left. + \frac{1}{2}\int_\Sigma \frac{\left(g_n - \mathcal{R}u\right)^2}{g_n} \right\}. \tag{2.12}$$

For (2.12) to be well-defined we assume an $L^\infty$ bound on $\tau_n$ such that $g_n$ is still positive. More precisely we assume that

$$0 < c_1 \leqslant g_n(\theta, s) \leqslant \|g\|_{L^\infty(\Sigma)} + \varepsilon, \text{ for all } n \geqslant 1, \tag{2.13}$$

which is the same as assuming that the perturbations $\tau_n$ are bounded from above by a small enough constant. Then, from the previous section, we have that both $F^n$ and $F$ are lower semicontinuous, strictly convex with unique minimizers $u_n$ and $u^*$ respectively. In a sense, we will prove that for a small change on our data g, our solution's behaviour does not change significantly. Before, we proceed with the stability analysis we need to ensure that the functional is indeed BV-coercive.

That is coercive with respect to the bounded variation norm $\|u\|_{BV(\Omega)} = \|u\|_{L^1(\Omega)} + |Du|(\Omega)$, rather than the total variation semi-norm only.

**Lemma 2.1.** *Let $g \in L^\infty(\Sigma)$ a strictly positive and bounded function, then the functional F in (2.1) is BV coercive i.e., there exists a constant $C > 0$ such that*

$$F(u) \geqslant C \, \|u\|_{BV(\Omega)} . \qquad (2.14)$$

**Proof.** Let $u \geqslant 0$ a.e with $u \in BV(\Omega)$ and consider $v = u - \bar{u}$. Then, by Hölder and Poincaré inequalities, one can prove that

$$\|v\|_{L^p(\Omega)} \leqslant C_1 \, |Dv|(\Omega)$$

and the corresponding estimate for the BV norm holds:

$$\|u\|_{BV(\Omega)} \leqslant \|\bar{u}\|_{L^1(\Omega)} + (C_1 + 1)|Dv|(\Omega). \qquad (2.15)$$

Note that in the above calculations we have used the fact that $|Du|(\Omega) = |Dv|(\Omega)$. Moreover, we know that there exists a constant $C_2 > 0$ such that

$$\|\mathcal{R}\bar{u}\|_{L^2(\Sigma)} = C_2 \, \|\bar{u}\|_{L^1(\Omega)}$$

since $\mathcal{R}\chi_\Omega \neq 0$ (see proof of theorem 2.2). Hence, we can derive the following bound:

$$F(u) \geqslant \alpha \, |Dv| \, (\Omega) + \frac{C_2 \, \|\bar{u}\|_{L^1(\Omega)}}{2 \, \|g\|_{L^\infty(\Sigma)}} \Big( C_2 \, \|\bar{u}\|_{L^1(\Omega)}$$
$$- 2 \Big( \|\mathcal{R}\| \, C_1 \, |Dv|(\Omega) + \|g\|_{L^\infty(\Sigma)} \Big) \Big). \qquad (2.16)$$

Setting

$$A = C_2 \, \|\bar{u}\|_{L^1(\Omega)} - 2 \Big( C_1 \, \|\mathcal{R}\| |Dv|(\Omega) + \|g\|_{L^\infty(\Sigma)} \Big)$$

we consider two cases:

(a) If $A \geqslant 1$, then using (2.15), (2.16), one can prove that

$$F(u) \left( \frac{C_1 + 1}{\alpha} + \frac{2 \, \|g\|_{L^\infty(\Sigma)}}{C_2} \right) \geqslant \|u\|_{BV(\Omega)} \qquad (2.17)$$

(b) If $A \leqslant 1$, then

$$\|\bar{u}\|_{L^1(\Omega)} \leqslant \frac{1 + 2 \Big( \|\mathcal{R}\| \, C_1 \, |Dv| + \|g\|_{L^\infty(\Omega)} \Big)}{C_2}$$

and using equation (2.15) we derive that:

$$\|u\|_{BV(\Omega)} - \frac{1 + 2 \, \|g\|_{L^2(\Sigma)}}{C_2} \leqslant \left( \frac{2C_1 \, \|\mathcal{R}\|}{C_2} + C_1 + 1 \right) |Dv| \leqslant \frac{K}{\alpha} F(u), \qquad (2.18)$$

where $K = \frac{2C_1 \, \|\mathcal{R}\|}{C_2} + C_1 + 1$. From equations (2.17), (2.18) we have that the functional $F$, is BV coercive. □

Moreover, we can prove that given constants $C > 0$ and $\varepsilon > 0$, there exists $n_0 \in \mathbb{N}$ such that

$$\left| F^n(u) - F(u) \right| \leqslant \epsilon \text{ for } n \geqslant n_0 \text{ and } \|u\|_{BV(\Omega)} \leqslant C. \qquad (2.19)$$

Indeed,

$$
\begin{aligned}
\left| F^n(u) - F(u) \right| &= \frac{1}{2c_1} \left( \left\| g + \tau_n - \mathcal{R}u \right\|_{L^2(\Sigma)}^2 - \left\| g - \mathcal{R}u \right\|_{L^2(\Sigma)}^2 \right) \\
&\leqslant \frac{1}{2c_1} \left( \left\| \tau_n \right\|_{L^2(\Sigma)}^2 + 2 \langle \tau_n, g - \mathcal{R}u \rangle \right) \\
&\leqslant \frac{1}{2c_1} \left\| \tau_n \right\|_{L^2(\Sigma)} \left( \left\| \tau_n \right\|_{L^2(\Sigma)} + 2 \| g \|_{L^2(\Sigma)} + 2 \| \mathcal{R}u \|_{L^2(\Sigma)} \right).
\end{aligned}
$$

The continuity of Radon transform in $L^2$ for functions with compact support, i.e.,

$$
\| \mathcal{R}u \|_{L^2}^2 \leqslant \left| S^{n-1} \right| (2r)^{n-1} \| u \|_{L^2}^2
$$

and $BV \hookrightarrow L^2$ continuously, imply that we can find an appropriate constant such that (2.19) is valid.

   With these preparations we can prove the following weak stability result for minimizers of (2.1).

**Theorem 2.3.** *Let $0 < u_n, u^* \in BV(\Omega)$ be the minimizers of the functionals $F^n$ and $F$ defined in (2.12) and (2.1) respectively. Then*

$$
u_n \rightharpoonup u^* \text{ in } L^2. \tag{2.20}
$$

**Proof.** Observe that $F^n(u_n) \leqslant F^n(u^*)$ and using (2.19) we have that

$$
\liminf_{n \to \infty} F^n(u_n) \leqslant \limsup_{n \to \infty} F^n(u_n) \leqslant F\left( u^* \right) < \infty
$$

lemma 2.1 implies that $(u_n)_{n \in \mathbb{N}}$ is BV bounded. Assume that (2.20) is not true, then there exists a subsequence $u_{n_k}$ which converges weakly to some $u \neq u^*$ in $L^2$. Hence,

$$
\begin{aligned}
F(u) &\leqslant \liminf_{n \to \infty} F(u_{n_k}) \\
&= \lim_{k \to \infty} \left( F^{n_k}(u_{n_k}) - F(u_{n_k}) \right) + \liminf_{k \to \infty} F^{n_k}(u_{n_k}) \\
&\leqslant F\left( u^* \right)
\end{aligned}
$$

which is a contradiction to the uniqueness of minimizer of $F$.                              $\square$

## 2.4. Error analysis using the Bregman distance

In the following we discuss a similar approach as presented in [12] for deriving an error estimate for our model (2.1) in terms of the Bregman distance. Let us note that what follows holds for the more general minimization problem

$$
\arg\min_{u \in X} \left\{ F(u) = \alpha J(u) + \beta J(\mathcal{R}u) + \frac{1}{2} \int_\Sigma \frac{(g - \mathcal{R}u)^2}{g} \right\}, \tag{2.21}
$$

where $J : X \to \mathbb{R}$ is a convex functional and $X$ is a Banach space such that $\mathcal{R} : X \to L^2(\Sigma) \cap X$ is a bounded operator. Before we proceed with proving an error

estimate for (2.21), we first recall the terminology of a minimizing solution, the source-condition and the Bregman distance for a convex functional.

**Definition 2.1.** An element $\tilde{u} \in X$ is called a minimizing solution of $\mathcal{R}u = g$ with respect to the functional $J: X \to \mathbb{R}$ if:

(i) $\mathcal{R}\tilde{u} = g$
(ii) $J(\tilde{u}) \leqslant J(v)$, $\forall\, v \in X$, $\mathcal{R}v = g$.

We consider the following source condition for an element $\tilde{u}$

$$\exists\, \widetilde{w} \in L^2(\Sigma) \text{ such that } \mathcal{R}^*\widetilde{w} \in \partial J(\tilde{u}), \tag{2.22}$$

where $\partial J(u)$ is the subdifferential of $J$ at $u$, see [16].

Next, we recall the Bregman distance for a convex functional $J$ together with some of its basic properties as it was introduced in [9].

**Definition 2.2.** Let $u, v \in X$ and $J: X \to \mathbb{R}$ convex functional, then the Bregman distance related to $J$, with $J(u) < \infty$, for all $u \in X$ is

$$D_J^p(u, v) := J(u) - J(v) - \langle p, u - v \rangle,\, p \in \partial J(v). \tag{2.23}$$

Now, we can derive an estimate for the difference of a minimizing solution $\tilde{u}$ in definition 2.1 and a regularized solution $\hat{u}$ of (2.21).

Let $\alpha > 0$, $\beta \geqslant 0$ and the data $g$ fulfil (2.2). Then, for a minimizer $\hat{u}$ of (2.21) and the exact solution $\tilde{u}$ satisfying $\mathcal{R}\tilde{u} = f$ with a fixed noise bound $\|g - f\|_{L^2(\Sigma)} \leqslant \delta$ from the exact data $f$, we have

$$\alpha J(\hat{u}) + \beta J(\mathcal{R}\hat{u}) + \frac{\|g - \mathcal{R}\hat{u}\|_2^2}{2\|g\|_{L^\infty}} \leqslant \alpha J(\tilde{u}) + \beta J(\mathcal{R}\tilde{u}) + \frac{\delta^2}{2c_1} \Leftrightarrow$$

$$\alpha D_J^{p_1}(\hat{u}, \tilde{u}) + \alpha < p_1, \hat{u} - \tilde{u} > + \beta D_J^{p_2}(\mathcal{R}\hat{u}, f)$$

$$+ \beta < p_2, \mathcal{R}\hat{u} - f > + \frac{\|g - \mathcal{R}\hat{u}\|_2^2}{2\|g\|_{L^\infty(\Sigma)}} \leqslant \frac{\delta^2}{2c_1},$$

where, we have used the corresponding Bregman distances related to the functional $J$ regarding the image and the sinogram regularization. Moreover, we require that

$$\partial(J(u) + J(\mathcal{R}u)) = \partial J(u) + \partial(J(\mathcal{R}u)) \tag{2.24}$$

holds, subject to the assumption that the related *effective domains* have a common point, that is

$$\mathrm{dom}J(u) \bigcap \mathrm{dom}J(\mathcal{R}u) \neq \varnothing \text{ for some } u \in X \tag{2.25}$$

In our case, this is valid due to theorem 2.1. Let

(i) $p_1 \in \partial J(\tilde{u})$
(ii) $p_2 \in \partial(J(\mathcal{R}\tilde{u})) = \mathcal{R}^*(\partial J(\mathcal{R}\tilde{u})) \in \mathcal{R}^*w_2$.

Moreover, assume that the source condition (2.22) is satisfied with respect to $J$, that is

$$\exists \, p_1 \in \partial J\left(\tilde{u}\right) \text{ s.t } p_1 = \mathcal{R}^* w_1 \, , \quad w_1 \in L^2(\Sigma).$$

Then, by generalized Young's inequality, for every $\varepsilon > 0$ we have

$$ab \leqslant \frac{a^2}{2\varepsilon} + \frac{\varepsilon b^2}{2}$$

and we conclude that

$$\alpha D_J^{p_1}\left(\hat{u}, \tilde{u}\right) + \beta D_J^{p_2}\left(\mathcal{R}\hat{u}, f\right) + \quad <\alpha w_1 + \beta p_2, \mathcal{R}\hat{u} - f> + \frac{\left\| g - \mathcal{R}\hat{u} \right\|_2^2}{2 \left\| g \right\|_{L^\infty(\Sigma)}} \leqslant \frac{\delta^2}{2c_1} \Leftrightarrow$$

$$\alpha D_J^{p_1}\left(\hat{u}, \tilde{u}\right) + \beta D_J^{p_2}\left(\mathcal{R}\hat{u}, f\right) + \quad \frac{\left\| g - \mathcal{R}\hat{u} \right\|_2^2}{2 \left\| g \right\|_{L^\infty(\Sigma)}} \leqslant \frac{\delta^2}{2c_1} + < \alpha w_1 + \beta p_2,$$

$$f - \mathcal{R}\hat{u} + g - g > \Leftrightarrow$$

$$\alpha D_J^{p_1}\left(\hat{u}, \tilde{u}\right) + \beta D_J^{p_2}\left(\mathcal{R}\hat{u}, f\right) + \quad \frac{\left\| g - \mathcal{R}\hat{u} \right\|_2^2}{2 \left\| g \right\|_{L^\infty(\Sigma)}} \leqslant \frac{\delta^2}{2c_1} + \frac{\left\| \alpha w_1 + \beta p_2 \right\|_2^2}{\varepsilon}$$

$$+ \quad \frac{\varepsilon}{2} \left\| g - \mathcal{R}\hat{u} \right\|_2^2 + \frac{\varepsilon \delta^2}{2} \Leftrightarrow \, .$$

Hence, for $\varepsilon = \left\| g \right\|_{L^\infty(\Sigma)}^{-1} > 0$ we have

$$D_J^{p_1}\left(\hat{u}, \tilde{u}\right) + \frac{\beta}{\alpha} D_J^{p_2}\left(\mathcal{R}\hat{u}, f\right) \leqslant \frac{\widetilde{c_1}\delta^2}{\alpha} + \alpha \left\| g \right\|_{L^\infty(\Sigma)} \left\| w_1 + \frac{\beta}{\alpha}\mathcal{R}^* w_2 \right\|_2^2.$$

We have proved the following theorem:

**Theorem 2.4.** *Let $\delta > 0$ be the noise bound related to the exact data f and the noise data g. Moreover let (2.24) hold. If $\hat{u}$ is a minimizer of (2.21) and $\tilde{u}$ the exact solution of $\mathcal{R}\tilde{u} = f$ which satisfies the source condition (2.22), then for $\alpha > 0, \beta \geqslant 0$ we have the following estimate:*

$$D_J^{p_1}\left(\hat{u}, \tilde{u}\right) + \frac{\beta}{\alpha} D_J^{p_2}\left(\mathcal{R}\hat{u}, f\right) \leqslant \frac{\widetilde{c_1}\delta^2}{\alpha} + \alpha \left\| g \right\|_{L^\infty(\Sigma)} \left\| w_1 + \frac{\beta}{\alpha}\mathcal{R}^* w_2 \right\|_2^2, \quad (2.26)$$

*where $\widetilde{c_1} = \frac{c_1 + \left\| g \right\|_{L^\infty(\Sigma)}}{2c_1 \left\| g \right\|_{L^\infty(\Sigma)}}$.*

For $\beta = 0$ theorem 2.4 recovers the same estimates presented in [6, theorems 1]. In the case $\beta > 0$ the additional term $\mathcal{R}^* w_2$, due to the source condition for total variation regularization on the sinogram, might give room for further improvement. It is a matter of future research to improve the estimate in (2.26), where we believe that in certain cases the term related to the sinogram regularization produces a better bound compared to no penalization on the projection space.

## 2.5. An explicit example of TV regularization on the sinogram

Before we continue with the numerical presentation, we discuss how a regularized solution in the projection space behaves in terms of an appropriate positive parameter $\beta$. In particular, we

derive an explicit solution of the weighted ROF minimization problem for the sinogram

$$\arg\min_{v \geqslant 0 \ \text{a.e}} \left\{ J(v) = \beta \, |Dv|(\Sigma) + \frac{1}{2} \int_{\Sigma} \frac{(g-v)^2}{g} \right\}, \tag{2.27}$$

where we consider,

$$u(x, y) = \begin{cases} 1, & \text{if } x^2 + y^2 \leqslant r \\ 0, & \text{otherwise} \end{cases} \tag{2.28}$$

$$g(\theta, s) = \mathcal{R}_\theta u(s) = \begin{cases} 2\sqrt{r^2 - s^2}, & \text{for } |s| < r \\ 0, & \text{otherwise.} \end{cases} \tag{2.29}$$

In figure 2(b), the given sinogram $g$ and the corresponding regularized solution $v$ of (2.27) for $\beta = 10$ is shown. We make the following Ansatz for a solution of (2.27)

$$v(s) = \begin{cases} \delta = g(\kappa), & \text{for } |s| \leqslant \kappa, \\ g(s), & \text{for } \kappa < |s| < r, \\ 0, & \text{otherwise.} \end{cases} \tag{2.30}$$

Note that, since $g \in C(-r, r)$, a solution $v$ of (2.27) is in $C(-r, r)$ and hence also in $W^{1,1}(-r, r)$ [13]. Therefore, $|Dv|(\Sigma) = \int_{\Sigma} |\nabla v| \, \mathrm{d}x$. Then, if we plug-in (2.30) in (2.27), we obtain

$$\arg\min_{v \geqslant 0 \ \text{a.e}} \left\{ \beta \, \|\nabla v\|_1 + \frac{1}{2} \int_{\Sigma} \frac{(g-v)^2}{g} \right\}$$

$$= \arg\min_{v \geqslant 0 \ \text{a.e}} \left\{ 4\beta\sqrt{r^2 - \kappa^2} + \int_0^\kappa \left( 2\sqrt{r^2 - s^2} + \frac{v^2}{2\sqrt{r^2 - s^2}} - 2v \right) \mathrm{d}s \right\}$$

which can be simplified to

$$\arg\min \kappa \left\{ (4\beta - 3\kappa)\sqrt{r^2 - \kappa^2} + \left( 3r^2 - 2\kappa^2 \right)\arcsin\left( \frac{\kappa}{r} \right) \right\}. \tag{2.31}$$

Numerically solving (2.31) under the constraint $0 < |\kappa| < r$, we obtain a value for $\kappa$ that we can substitute in (2.30) and find the corresponding value of our solution after the regularization. We solve (2.31) with MATLAB's built-in routine *fminbnd* in $\kappa \in [0, r)$. In figure 3, we present how the $\beta$ parameter relates to the constant height value $\delta$ of the computed regularized solution. Clearly, for small values of $\beta$, there is no significant effect of the total variation regularization but as we increase $\beta$ we have that $\delta$ decreases to zero, while $\kappa$ tends to $r$.

Before we apply the inverse Radon transform on (2.30) and find the corresponding solution in the image space, we need to verify its optimality. The following theorem ensures that the candidate solution (2.30) for the problem (2.27) is indeed optimal.

**Theorem 2.5.** *The unique solution of the minimization problem (2.27) is defined by (2.30).*

(a)

(b)
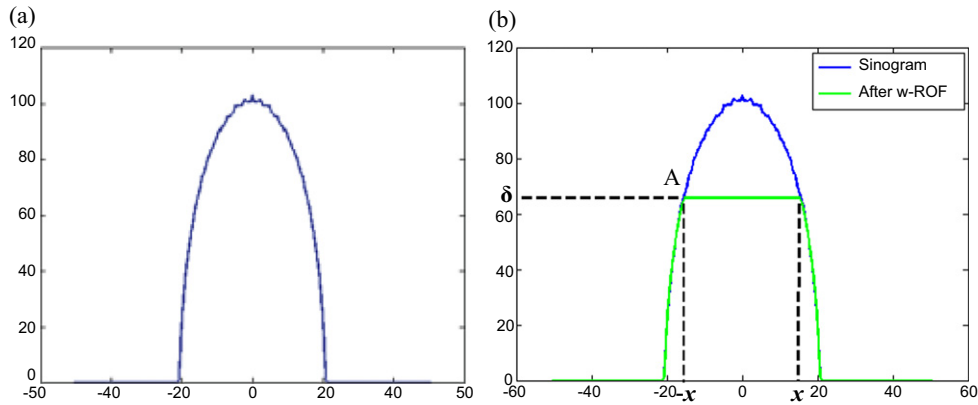
**Figure 2.** The original sinogram $g$ with $r = 50.5$, plotted at 45 degrees in (a) and the regularized sinogram $v$ with $\beta = 10$ in (b).
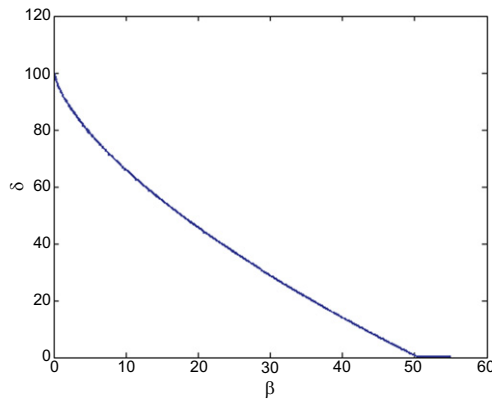
**Figure 3.** The relation between the regularization parameter $\beta$ and $\delta$ in (2.30), computed using (2.31) for the example in figure 2. The parameter $\beta$ varies from 0.001 to 55 with step size 0.1.

**Proof.** The optimality condition on (2.27) implies that:

$$0 \in \partial J(u) \Leftrightarrow \beta q + \frac{v - g}{\sqrt{g}} = 0, \quad q \in \partial |Du|(\Omega). \tag{2.32}$$

We can characterize the subdifferential of total variation, see [7], as

$$\partial |Du|(\Sigma) = \left\{ \operatorname{div} p \colon p \in C_o^\infty(\Sigma), \ \|p\|_\infty \leqslant 1, \ \langle \operatorname{div} p, v \rangle = |Du|(\Sigma) \right\}. \tag{2.33}$$

Therefore, in our case (2.32) becomes

$$\beta p'(s) + \frac{v(s) - g(s)}{\sqrt{g(s)}} = 0, \quad \text{in } s \in \Sigma \tag{2.34}$$

with $-1 \leqslant p(s) \leqslant 1$ and $\int_\Sigma p'(s) v(s) = \int_\Sigma |v'(s)|$. If v is either increasing or decreasing on an interval $I \subset \Sigma$, then through integration by parts one obtains $p(s) v'(s) = |v'(s)|$ which

15
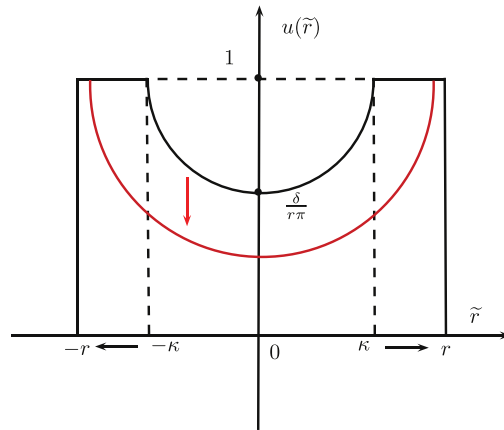
**Figure 4.** The solution $u(\tilde{r})$ (solid line) given in (2.38) inside the interval $[-r, r]$ and zero outside. The black and the red curve constitute the regularized solution for a smaller and larger value of $\beta$, respectively. The larger $\beta$ the more the solution concentrates around the boundaries of the disc.

immediately implies that $p' = 0$ and $v = g$ on I. However, when $v \neq g$ on an interval $I' \subset \Sigma$, then $p' \neq 0$ which is true only if $v'(s) = 0$ on $I'$, i.e., v is constant.

For computing the regularized image that corresponds to a solution of (2.27) we first note that the rotational symmetry of the object in image space allows to simplify the Radon transform and its inverse. In this case the Radon transform coincides with the so-called *Abel transform*, see [26, chapter 8]. More precisely, if $u$ is a radial function and $u(x, y) = f\left(\sqrt{x^2 + y^2}\right)$ we have

$$\mathcal{R}_\theta u(s) = 2 \int_s^\infty \frac{f(r)r}{\sqrt{r^2 - s^2}} \mathrm{d}r. \tag{2.35}$$

Using (2.35), we can recover analytically the solution $u$ for a regularized sinogram (2.30).

The Abel transform and the inverse Abel transform in this case are

$$\mathcal{A}\left(u(\tilde{r})\right)(x) = 2 \int_x^\infty \frac{\tilde{r}u(\tilde{r})}{\sqrt{\tilde{r}^2 - x^2}} \mathrm{d}\tilde{r} \tag{2.36}$$

$$u(\tilde{r}) = -\frac{1}{\tilde{r}\pi} \frac{\mathrm{d}}{\mathrm{d}\tilde{r}} \int_{\tilde{r}}^\infty \frac{r\mathcal{A}\left(u(\tilde{r})\right)(x)}{\sqrt{x^2 - r^2}} \mathrm{d}x. \tag{2.37}$$

Setting $u(\tilde{r}) = 1$ and replacing the upper limit of the integral $\infty$ by $r$ in (2.36), the expression in (2.36) matches the expression for the Radon transform in (2.29). Therefore, we plug-in (2.30) in (2.37) and focus on the constant part of the sinogram for $-\kappa \leqslant \tilde{r} \leqslant \kappa$,

$$u(\tilde{r}) = -\frac{1}{\tilde{r}\pi} \frac{\mathrm{d}}{\mathrm{d}\tilde{r}} \int_{\tilde{r}}^r \frac{x\delta}{\sqrt{x^2 - \tilde{r}^2}} \mathrm{d}x = \frac{\delta}{\pi\sqrt{r^2 - \tilde{r}^2}}. \tag{2.38}$$

We observe that the reconstructed image is affected by the initial loss of contrast $\delta$ of the sinogram regularization in (2.30) and depends radially on $\tilde{r}$. In figure 4, we present the

regularized solution $u$ for two values of $\beta$. Recall, as we increase $\beta$ (red curve), we have that $\delta \to 0$ and $\kappa \to r$.

## 3. Numerical implementation

In this section we discuss the numerical solution of the minimization problem (2.1). We employ the split Bregman technique [19] which separates the problem into two subproblems —one in image space and one in projection space—that are solved iteratively in an alternating fashion. In order to present the numerical solution we start with formulating (2.1) in a discrete setting.

### 3.1. Discrete setting

Let $(u_{i,j})$, $i = 1, \ldots, m$, $j = 1, \ldots, n$ be the discretized image defined on a rectangular grid of size $m \times n$, $m, n > 0$, and $(v_{i,j})$, $i = 1, \ldots, k$, $j = 1, \ldots, l$ the discretization for an element in the sinogram space $\Sigma = [0, \pi) \times [-r, r]$ where k denotes the number of lines and l the number of angles. The values $u_{i,j}$ and $v_{i,j}$ are defined on two-dimensional grids. They are rearranged into one-dimensional vectors $u \in \mathbb{R}^{nm}$ and $v \in \mathbb{R}^{kl}$ by appending the columns of the array to each other, starting from the leftmost. Then, the discrete gradient for $u \in \mathbb{R}^{m \times n}$ is a matrix $\nabla \in \mathbb{R}^{2\,nm \times nm}$ which is the standard forward difference approximation of the gradient in the continuum. More precisely, applying the discrete gradient to $u$ gives $\nabla u = ((\nabla u)_1, (\nabla u)_2) \in \mathbb{R}^{2\,nm}$ with

$$(\nabla u)_1(i, j) = \begin{cases} u(i, j + 1) - u(i, j), & \text{if } 1 \leqslant i \leqslant n, 1 \leqslant j < m, \\ 0, & \text{if } 1 \leqslant i \leqslant n, j = m. \end{cases}$$

$$(\nabla u)_2(i, j) = \begin{cases} u(i + 1, j) - u(i, j), & \text{if } 1 \leqslant i < n, 1 \leqslant j \leqslant m, \\ 0, & \text{if } i = n, 1 \leqslant j \leqslant m. \end{cases}$$

The discrete divergence is defined as its adjoint, see [14], and is given by

$$\text{div}: \mathbb{R}^{2\,nm} \to \mathbb{R}^{nm} \text{ with div} (z) \cdot u = -z \cdot \nabla u.$$

Further, to approximate the Radon transform $\mathcal{R}$ we introduce the discrete Radon transform as a mapping $R: \mathbb{R}^{nm} \to \mathbb{R}^{kl}$ and its inverse $R^{-1}: \mathbb{R}^{kl} \to \mathbb{R}^{nm}$. In the numerical implementation the discrete Radon transform is represented by a sparse matrix $R \in \mathbb{R}^{kl \times nm}$ which acts on $u \in \mathbb{R}^{nm}$ to obtain a sinogram image $v \in \mathbb{R}^{kl}$. Defining $x(\theta_{\hat{i}}, s_{\hat{j}})$, $\hat{i} = 1, \ldots, k$, $\hat{j} = 1, \ldots, l$, the line defined by $\theta_{\hat{i}}, s_{\hat{j}}$, we can define for $i = 1, \ldots, m$ and $j = 1, \ldots, n$

$$\psi_{i,j}\left(\theta_{\hat{i}}, s_{\hat{j}}\right) = \begin{cases} 1, & \text{where the line } x\left(\theta_{\hat{i}}, s_{\hat{j}}\right) \text{ goes through the pixel } (i, j) \\ 0, & \text{otherwise.} \end{cases} \tag{3.1}$$

Using this notation and the linearity of the Radon transform, we define the discrete Radon transform as

$$Ru\left(\theta_{\hat{i}}, s_{\hat{j}}\right) = \sum_{i=1}^{m} \sum_{j=1}^{n} u_{i,j} \mathcal{R}\psi_{i,j}\left(\theta_{\hat{i}}, s_{\hat{j}}\right), \tag{3.2}$$

where $\mathcal{R}\psi_{i,j}(\theta_{\hat{i}}, s_{\hat{j}})$ is equal to the length of the intersection of the projection line with the pixel $(i,j)$.

With these discrete quantities we define the discrete functional $F$ by

$$F(u) = a \parallel \nabla u \parallel_1 + \beta \parallel (\nabla Ru) \parallel_1 + \frac{1}{2} \sum_{k,l} \frac{(g - \mathcal{R}u)^2}{g}, \tag{3.3}$$

and the discrete version of the minimization problem (2.1)

$$\min_{u \in \mathbb{R}^{m \times n}} F(u). \tag{3.4}$$

### 3.2. Split Bregman algorithm

To solve the problems defined in (3.3) we employ the Bregman iteration [25] combined with a splitting technique. The resulting algorithm is called Split Bregman method which is proposed in [19] to efficiently solve total variation and $\ell_1$ regularized image processing problems. The idea of this splitting procedure is to replace a complex and costly minimization problem by a sequence of simple and cheaply to solve minimization problems and to set up an iteration in which they are solved alternatingly. Note, that the Split Bregman method can be equivalently phrased in terms of an augmented Lagrange method and Douglas–Rachford splitting, see [17, 32, 33].

We follow [19] to adapt the Split Bregman algorithm to the solution of (2.1). To do so, we consider

$$\min_{\{u: \ u \geqslant 0 \ \text{a.e.}\}} \alpha \parallel \nabla u \parallel_1 + \beta \parallel \nabla (Ru) \parallel_1 + \frac{1}{2} \sum_{k,l} \frac{(g - Ru)^2}{g}. \tag{3.5}$$

We start with replacing (3.5) by an equivalent constrained minimization problem for two unknowns, the image $u \in \mathbb{R}^{m \times n}$ and the sinogram $v \in \mathbb{R}^{k \times l}$, related to each other by $v = Ru$. This gives

$$\min_{\{(u,v): \ u \geqslant 0 \ \text{a.e.}\}} \alpha \parallel \nabla u \parallel_1 + \beta \parallel \nabla v \parallel_1 + \frac{1}{2} \sum_{k,l} \frac{(g - v)^2}{g} \ \text{s.t} \ v = Ru. \tag{3.6}$$

For computational efficiency reasons, we introduce three additional variables

$$z = \nabla u, \ w = \nabla v \ \text{and} \ u = \tilde{u} \tag{3.7}$$

and rephrase (3.6) again into

$$\min_{\left\{(u,\tilde{u},v,z,w): \ \tilde{u} \geqslant 0 \ \text{a.e., satisfying (3.7)}\right\}} \alpha \parallel z \parallel_1 + \beta \parallel w \parallel_1 + \frac{1}{2} \sum_{k,l} \frac{(g - v)^2}{g}. \tag{3.8}$$

Then, we could iteratively solve the constrained minimization problem (3.8) by Bregman iteration. Starting with initial conditions $b_1^0 \in \mathbb{R}^{k \times l}$, $b_2^0 \in \left(\mathbb{R}^{k \times l}\right)^2$, $b_3^0 \in \left(\mathbb{R}^{m \times n}\right)^2$, $b_4^0 \in (\mathbb{R}^{m \times n})$ we iteratively solve for $k = 0, 1, \ldots$

$$\arg \min_{u,\tilde{u},v,z,w} \left\{ \alpha \parallel z \parallel_1 + \beta \parallel w \parallel_1 + \sum \frac{(g-v)^2}{g} + \iota_{(\tilde{u}>0)} \right.$$

$$+ \frac{\lambda_1}{2} \left\| b_1^k + \mathcal{R}u - v \right\|_2^2 + \frac{\lambda_2}{2} \left\| b_2^k + \nabla v - w \right\|_2^2$$

$$\left. + \frac{\lambda_3}{2} \left\| b_3^k + \nabla u - z \right\|_2^2 + \frac{\lambda_4}{2} \left\| b_4^k + u - \tilde{u} \right\|_2^2 \right\}$$

$$b_1^{k+1} = b_1^k + \mathcal{R}u^{k+1} - v^{k+1} \qquad b_2^{k+1} = b_2^k + \nabla v^{k+1} - w^{k+1}$$

$$b_3^{k+1} = b_3^k + \nabla u^{k+1} - z^{k+1} \qquad b_4^{k+1} = b_4^k + u^{k+1} - \tilde{u}^{k+1},$$

with Lagrange multipliers $(\lambda_i)_{i=1}^4 > 0$, $b_1^k \in \mathbb{R}^{k \times l}$, $b_2^k \in \left(\mathbb{R}^{k \times l}\right)^2$, $b_3^k \in \left(\mathbb{R}^{m \times n}\right)^2$ and $b_4^k \in (\mathbb{R}^{m \times n})$ and $\iota_{(\tilde{u}>0)}$ being the characteristic function for the positivity constraint on $\tilde{u}$. To progress, in each iteration above we would need to solve a minimization problem in all $u$, $\tilde{u}$, $v$, $z$, $w$ at the same time which is numerically very involved. Instead, we use the split Bregman idea of [19] and in each iteration solve a sequence of decoupled problems in $u$, $\tilde{u}$, $v$, $z$, $w$, that is

$$v^{k+1} = \arg \min_v \left\{ \frac{1}{2} \sum \frac{(g-v)^2}{g} + \frac{\lambda_1}{2} \left\| b_1^k + \mathcal{R}u^k - v \right\|_2^2 \right.$$

$$\left. + \frac{\lambda_2}{2} \left\| b_2^k + \nabla v - w^k \right\|_2^2 \right\} \qquad (3.9)$$

$$u^{k+1} = \arg \min_u \left\{ \frac{\lambda_1}{2} \left\| b_1^k + \mathcal{R}u - v^{k+1} \right\|_2^2 + \frac{\lambda_3}{2} \left\| b_3^k + \nabla u - z^k \right\|_2^2 \right.$$

$$\left. + \frac{\lambda_4}{2} \left\| b_4^k + u - \tilde{u}^k \right\|_2^2 \right\} \qquad (3.10)$$

$$\tilde{u}^{k+1} = \arg \min_{\tilde{u}} \left\{ \iota_{(\tilde{u}>0)} + \frac{\lambda_4}{2} \left\| b_4^k + u^{k+1} - \tilde{u} \right\|_2^2 \right\} \qquad (3.11)$$

$$z^{k+1} = \arg \min_z \left\{ \alpha \parallel z \parallel_1 + \frac{\lambda_3}{2} \left\| b_3^k + \nabla u^{k+1} - z \right\|_2^2 \right\} \qquad (3.12)$$

$$w^{k+1} = \arg \min_w \left\{ \beta \parallel w \parallel_1 + \frac{\lambda_2}{2} \left\| b_2^k + \nabla v^{k+1} - w \right\|_2^2 \right\} \qquad (3.13)$$

$$b_1^{k+1} = b_1^k + \mathcal{R}u^{k+1} - v^{k+1} \qquad (3.14)$$

$$b_2^{k+1} = b_2^k + \nabla v^{k+1} - w^{k+1} \qquad (3.15)$$

$$b_3^{k+1} = b_3^k + \nabla u^{k+1} - z^{k+1} \qquad (3.16)$$

$$b_4^{k+1} = b_4^k + u^{k+1} - \tilde{u}^{k+1}. \qquad (3.17)$$

This procedure leads to five minimization problems that have to be solved sequentially in each iteration. Every one of them either has an explicit solution or involves the solution of a linear system of equations that can be efficiently solved with an iterative method such as conjugate gradient. We iterate until

$$\frac{\left\| \tilde{u}^{K+1} - \tilde{u}^{K} \right\|_2^2}{\left\| \tilde{u}^{K+1} \right\|_2} < 10^{-4}$$

and take $v^{K+1}$ as the regularized sinogram and $\tilde{u}^{K+1}$ as the reconstructed image. Let us go into more detail on the solution of each minimization problem. Solution of (3.9): to solve (3.9) we derive the corresponding Euler–Lagrange equation for $v$ and obtain a linear system of equations with $k \cdot l$ unknowns $v_{i,j}$, $i = 1, \ldots, k$, $j = 1, \ldots, l$ which reads

$$(39) \Rightarrow \left( (1 + \lambda_1)g - \lambda_2 g \, \mathrm{div} \cdot \nabla \right)v = g + \lambda_1 g \left( b_1^k + Ru^k \right) + \lambda_2 g \, \mathrm{div} \left( b_2^k - w^k \right) \quad (3.18)$$

The system (3.18) is solved by a conjugate gradient method. Solution of (3.10): the Euler–Lagrange equation of (3.10) for $u$ reads

$$(3.10) \Rightarrow \left( \lambda_1 R^* R - \lambda_3 \, \mathrm{div} \cdot \nabla + \lambda_4 \right)u$$
$$= \lambda_1 R^* \left( v^{k+1} - b_1^k \right) + \lambda_3 \, \mathrm{div} \left( b_3^k - z^k \right) - \lambda_4 \left( b_4 - \tilde{u}^k \right) \quad (3.19)$$

where $R^*$ is the adjoint of $R$, that is the discrete backprojection. As before, the system (3.19) is solved by a conjugate gradient method. Solution of (3.11): the solution of (3.11) is given by

$$\tilde{u}^{k+1} = \max \left\{ b_4^{k+1} + u^{k+1}, 0 \right\}.$$

Solution of (3.12) and (3.13): finally, the solution of the minimization problems (3.12), (3.13) can be obtained exactly through soft shrinkage. That is,

$$z^{k+1} = S_{\frac{\alpha}{\lambda_3}} \left( b_3^k + \nabla u^{k+1} \right) := \max \left( \left\| b_3^k + \nabla u^{k+1} \right\|_2 - \frac{\alpha}{\lambda_3}, 0 \right) \frac{b_3^k + \nabla u^{k+1}}{\left\| b_3^k + \nabla u^{k+1} \right\|_2} \quad (3.20)$$

$$w^{k+1} = S_{\frac{\beta}{\lambda_2}} \left( b_2^k + \nabla v^{k+1} \right) := \max \left( \left\| b_2^k + \nabla v^{k+1} \right\|_2 - \frac{\beta}{\lambda_2}, 0 \right) \frac{b_2^k + \nabla v^{k+1}}{\left\| b_2^k + \nabla v^{k+1} \right\|_2}. \quad (3.21)$$

## 4. Numerical results

In this section, we present our results on both simulated and real PET data. The Radon matrix that we described in (3.2) is fixed and produces sinograms of size $192 \times 192$, that is the sinogram is given in 192 projection lines, 192° degrees with 1° degree incrementation and the corresponding reconstructed image is of size $175 \times 175$ pixels. We corrupt the sinograms with Poisson noise of different levels. In order to create noisy images corrupted by Poisson noise, we apply the MATLAB routine *imnoise* (sinogram, *poisson*). MATLAB's *imnoise* function acts in the following way: for an image of double precision, the input pixel values are interpreted as means of a Poisson distribution scaled by a factor of $10^{-12}$. For example, if an input pixel has the value $5.5 * 10^{-12}$ then the corresponding output pixel will be generated from a Poisson distribution with mean of 5.5 and afterwards scaled back to its original range by $10^{12}$. The factor $10^{12}$ is fixed to represent the maximal number of detectable photons. Our simulated sinograms are in $[0, 1]$ intensity and in order to create different noise levels, we have to rescale the initial sinogram with a suitable factor before applying *imnoise* and then scale it back with the same factor, i.e., *Noisy Sinogram = scale \* imnoise* $\left( \frac{sinogram}{scale}, poisson \right)$.

(a): 2 discs

(c): Low Noise: SNR=18.5246

(b): Noiseless Sinogram

(d): High Noise: SNR=8.6814
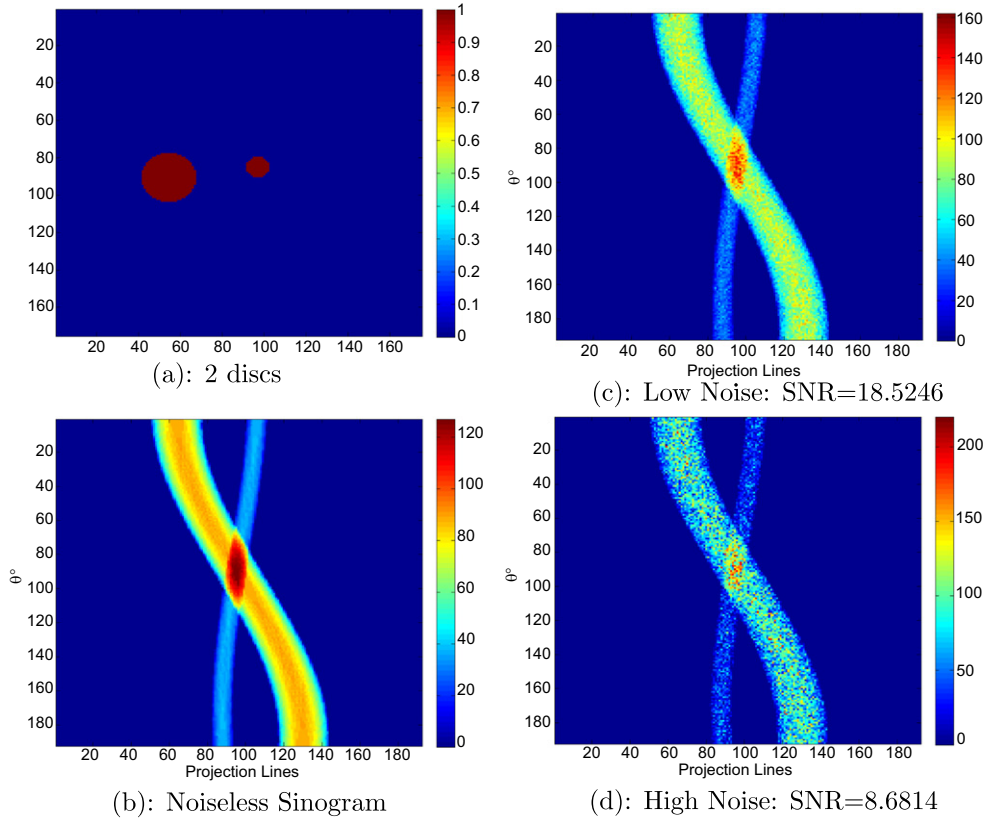
**Figure 5.** The phantom image includes two discs of radius $r_1 = 26$ and $r_2 = 11$ pixels. Its sinogram has 192 angles and 192 rays with low and high noise.

To simulate realistic sinograms with higher noise level, we use $10^{13}$ as a scaling factor, see for example figure 5. The real data was obtained from the hardware phantom 'Wilhelm', a self-built phantom modelled of the human body. Beside the activity in the heart a small source is placed in the phantom to simulate a lesion, see section 4.1 for more information.

Before presenting our results we give some specifics on how equations (3.9)-(3.13) are solved and how parameters are chosen. Both linear systems (3.18) and (3.19) are solved using MATLAB's built-in function *cg* which performs a conjugate gradient method. As a stopping criterium we either stop after at most 200 iterations or if the relative residual is smaller than $10^{-3}$. As it is observed in [19], it seems optimal to apply only a few steps of an iterative solver for both subproblems (3.18) and (3.19) since the error in the split Bregman algorithm is updated in every iteration.

The Lagrange multiplies $(\lambda_i)_{i=1}^4$ in equations (3.9)–(3.13) in section 3.2 are chosen following [18] to optimize convergence speed and well conditioning. They were fixed as $\lambda_1 = 0.001$, $\lambda_2 = 1$, and $\lambda_3 = \lambda_4 = 100$. Note that these parameters may affect the condition number for both system matrices

$$A_{img} = \lambda_1 R^*R - \lambda_3 \operatorname{div} \cdot \nabla + \lambda_4 I$$
$$A_{\sin} = (1 + \lambda_1)g - \lambda_2 g \operatorname{div} \cdot \nabla$$

in (3.18) and (3.19) and hence the convergence rates of iterative solvers used to solve them are affected by this choice.

Finally, we observe that after 150 Split Bregman iterations, there are no significant changes in the reconstructed image and therefore we choose a stopping criteria of either at most $K = 400$ iterations or we stop at iteration $K$ where for the first time we have

$$\frac{\left\| \widetilde{u}^{K+1} - \widetilde{u}^{K} \right\|_2}{\left\| \widetilde{u}^{K+1} \right\|_2} < 10^{-4},$$

where $\widetilde{u}^{K+1}$ the regularized image. To evaluate the quality of reconstructed images we choose the *signal-to-noise ratio* (SNR) as a quality measure. The SNR is defined as

$$SNR = 20 \log\left( \frac{\| u \|_2}{\| u - \widetilde{u} \|_2} \right), \tag{4.1}$$

where $u$ and $\widetilde{u}$ denote the ground truth and the reconstructed image, respectively. In what follows, we first evaluate the proposed reconstruction technique (2.1) against pure total variation regularization on the image ($\beta = 0$) for a synthetic image of two circles and for different noise levels, as well as for a real data set acquired for the Wilhelm phantom. Then, we numerically analyse the scale space properties of pure sinogram regularization, that is for $\alpha = 0$, which will be a motivation for the final section in which we discuss the merit of the proposed reconstruction method for PET data that encodes thin image structures.

### 4.1. Image reconstruction from corrupted simulated and real PET data

We start with a discussion of numerical results obtained for simulated PET data. Figure 5 shows a simulated phantom of two discs with different radius and the corresponding noiseless and noisy sinograms corrupted with low and high level Poisson noise as described above.

First, we evaluate the proposed algorithm for reconstructing an image from the sinogram corrupted by low level Poisson noise with SNR = 18.5246, see figure 5(c). The proposed reconstruction algorithm with joint total variation regularization of image and sinogram (that is $\alpha, \beta > 0$) is compared with the algorithm that uses pure total variation regularization of the image (that is $\alpha > 0$ and $\beta = 0$). Both reconstruction strategies are tested for a range of parameters $\alpha$, $\beta$ and in each case the reconstruction is found which has the highest SNR value. For $\beta = 0$ we computed the reconstructed image for $\alpha = 3, 4, 5, 6, 7$. The optimal reconstructed image in terms of the best SNR = 25.8589 is obtained for $\alpha = 6$, see figure 6. Then, we test the proposed reconstruction method applying total variation regularization on both the image and the sinogram using the same range of $\alpha = 3, 4, 5, 6, 7$ and $\beta = 0.001, 0.005, 0.01, 0.05$. Here, the optimal reconstruction was obtained for $\alpha = 6$ and $\beta = 0.001$ with SNR = 25.3127, see figure 6. In table 1 a full list of tested parameters and SNRs for corresponding reconstructed images is given. The results do not indicate a significant difference between the algorithm with and without total variation regularization on the sinogram, both visually and also in terms of the SNR. Indeed, in the low noise case additional total variation regularization on the sinogram produces even slightly worse results in terms of SNR than using no regularization on the sinogram at all.
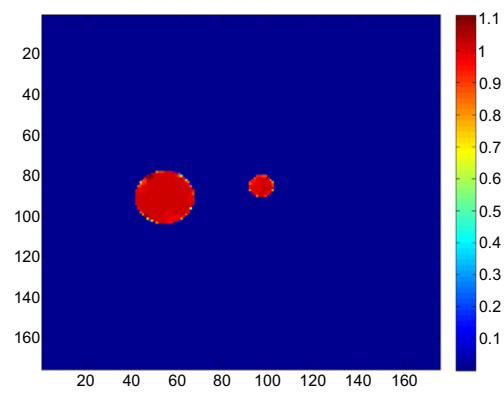
(a): $\alpha = 6$, $\beta = 0$
SNR=25.8589
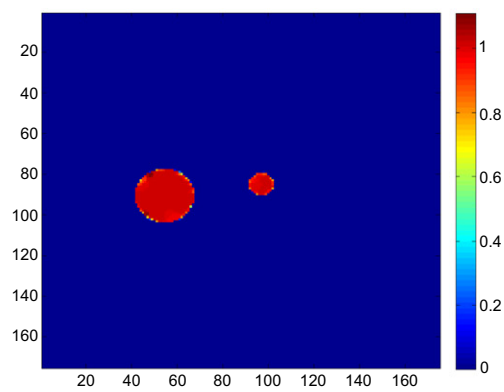


(b): $\alpha = 6$, $\beta = 10^{-3}$
SNR=25.3127
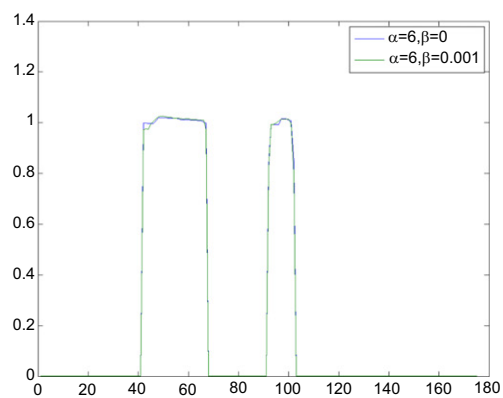


(c): Middle line profiles

**Figure 6.** Low level noise: optimal reconstruction results of the two discs image with sinogram shown in figure 5(c) with and without sinogram regularization and a comparison of the line profiles for the two results.

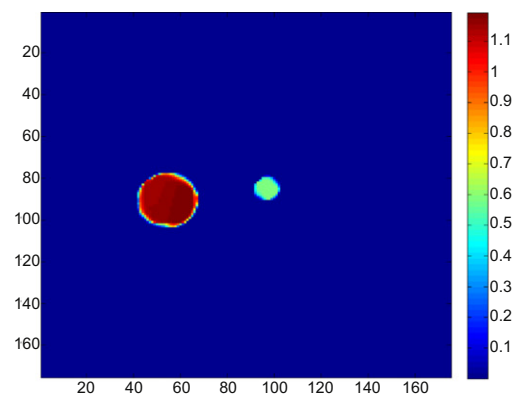**Table 1.** Low level noise for simulated example in figure 5: SNRs of reconstructed images for different combinations of $\alpha$ and $\beta$ values.

|   |   | $\beta$ | | | | | |
|---|---|---|---|---|---|---|---|
|   |   | 0 | 0.001 | 0.005 | 0.01 | 0.05 | 0.1 |
| $\alpha$ | 3 | 24.0819 | 22.0172 | 22.4415 | 22.8894 | 23.2414 | 21.6533 |
|   | 4 | 25.3682 | 24.0926 | 24.2951 | 24.4801 | 23.6303 | 21.9382 |
|   | 5 | **25.7867** | 25.0829 | 25.0779 | 25.0469 | 23.9432 | 22.0367 |
|   | 6 | **25.8589** | **25.3127** | 24.7787 | 25.0602 | 24.0095 | 22.1034 |
|   | 7 | 25.7436 | 24.8499 | 24.8278 | 25.0148 | 23.9662 | 22.2289 |

**Table 2.** High level noise for simulated example in figure 5: SNRs of reconstructed images for different combinations of $\alpha$ and $\beta$ values.

|   |   | $\beta$ | | | | | |
|---|---|---|---|---|---|---|---|
|   |   | 0 | 0.001 | 0.005 | 0.01 | 0.05 | 0.1 |
| $\alpha$ | **250** | **10.9544** | **10.9665** | 10.9557 | 10.9464 | 10.8531 | 10.8058 |
|   | 275 | 10.9502 | 10.9599 | 10.9501 | 10.9381 | 10.8595 | 10.8013 |
|   | **300** | **10.9425** | 10.9543 | 10.9415 | 10.9257 | 10.8267 | 10.7777 |
|   | 325 | 10.9167 | 10.9551 | 10.9434 | 10.9283 | 10.8101 | 10.7293 |
|   | 350 | 10.8784 | 10.9289 | 10.9165 | 10.9014 | 10.7946 | 10.7104 |

The TV regularization on the sinogram gains importance in the reconstruction algorithm when the noise in the corruption of the sinogram is increased. The sinogram with high level noise is shown in figure 5(d) and has SNR = 8.6814. We tested the proposed method for $\alpha = 250, 275, 300, 325, 350$ and $\beta = 0, 0.001, 0.01, 0.05, 0.1$. The results are reported in table 2.

The highest SNR is obtained when $\alpha = 250$ and $\beta = 0.001$, see figure 7(b). Although, it is hard to distinguish any difference between the cases of $\beta$, we observe that the extra penalization on the sinogram produces better results in terms of the SNR value, see figure 7. The increase in SNR for $\beta > 0$ can be seen when comparing the middle line profiles of the reconstructed images with and without sinogram regularization in figure 7(c).

As a second example for our evaluation of the algorithm for PET reconstruction we consider real PET data obtained from scanning a self-built phantom of a human breast with a small source which simulates a lesion, compare figure 8(a). The data has been acquired with a Siemens Biograph Sensation 16 PET/CT scanner (Siemens Medical Solutions) located at the University Hospital in Münster. From the 3D PET data we used only one sinogram slice. The 2D sinogram dimension is $192 \times 192$ with a pixel size of $3.375 \, \text{mm}^2$. The size of the reconstructed image is $175 \times 175$, covering a field of view of 590.625 mm in diameter. The 2D slice of the noisy sinogram which has been used in our computations is shown in figure 8(b). Reconstructions obtained from the proposed algorithm, with and without sinogram regularization, are shown in figure 9. The additional regularization of the sinogram seems to allow for smoother image structures (such as the boundary of the red lesion) and results in a slight reduction of the stair casing effect of total variation regularization.
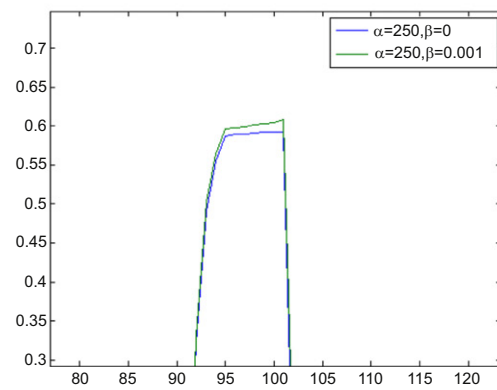
In the following two sections we will aim to improve our understanding of this new sinogram regularization, taking the analytic solution of section 2.5 as a starting point. A thorough numerical discussion of this example in section 4.2 leeds us to section 4.3 where the

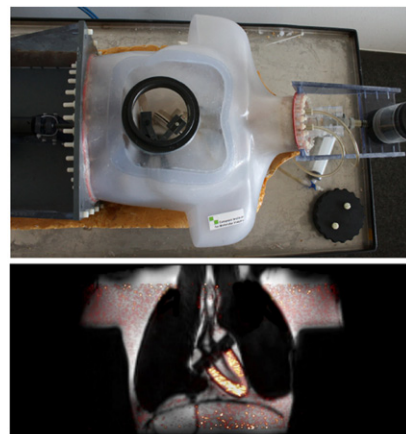(a): $\alpha = 250$, $\beta = 0$
SNR=10.9544
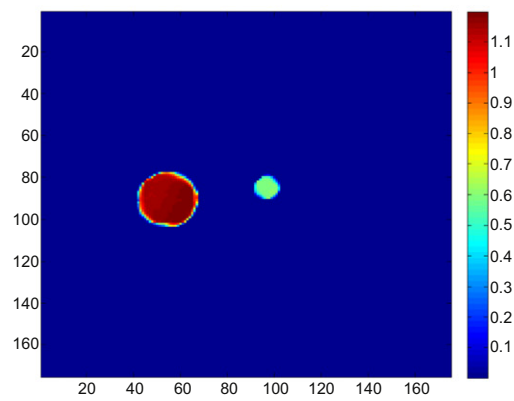


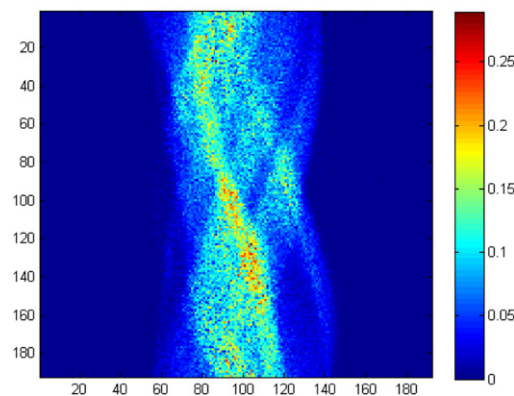(b): $\alpha = 250$, $\beta = 10^{-3}$
SNR=10.9665



(c): Zoom In: Middle line profiles

**Figure 7.** High level noise for simulated example in figure 5: best SNRs with/without total variation regularization on the sinogram and the middle line profiles of the reconstructed images.

(a)



(b)

**Figure 8.** Real PET data.

benefits of total variation regularization of the sinogram for the reconstruction of thin objects are discussed.

## 4.2. Scale space of sinogram regularization

Following up on the computations in section 2.5, we now discuss how the regularization on the sinogram effects the backprojected image. Let us recall that every point $(\theta, s)$ on the sinogram corresponds to a line $s = x \cos \theta + y \sin \theta$ that passes through a point $(x,y)$ on the image, with a distance $s$ from the origin and normal to the direction $(\cos \theta, \sin \theta)$. Moreover (compare Thirion [34]), every point on an edge in the sinogram corresponds to a line in the object space which is tangent to the boundary of the object. To further understand how sinogram regularization acts, we consider the effect of the regularization when reconstructing an image from simulated noise-free Radon data. To this end we set $\alpha = 0$, regularize the noise-free sinogram with different values of $\beta$, and apply FBP to the regularized sinogram to obtain the corresponding reconstructed image. We call the set of reconstructed images from regularized sinograms with varying $\beta$ regularization, the scale space of total variation regularization of the sinogram.
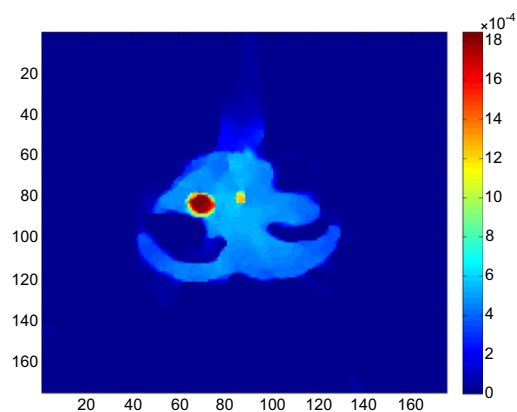
(a): $\alpha = 5, \beta = 0$
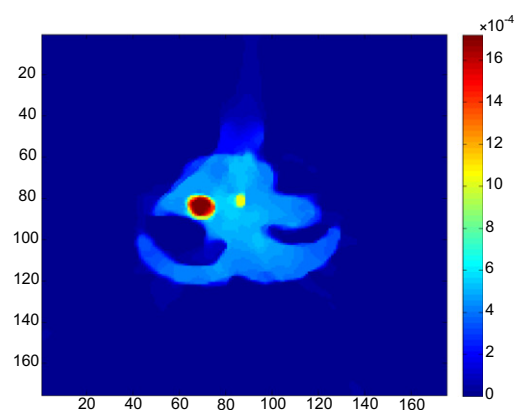


(b): $\alpha = 4, \beta = 0.1$

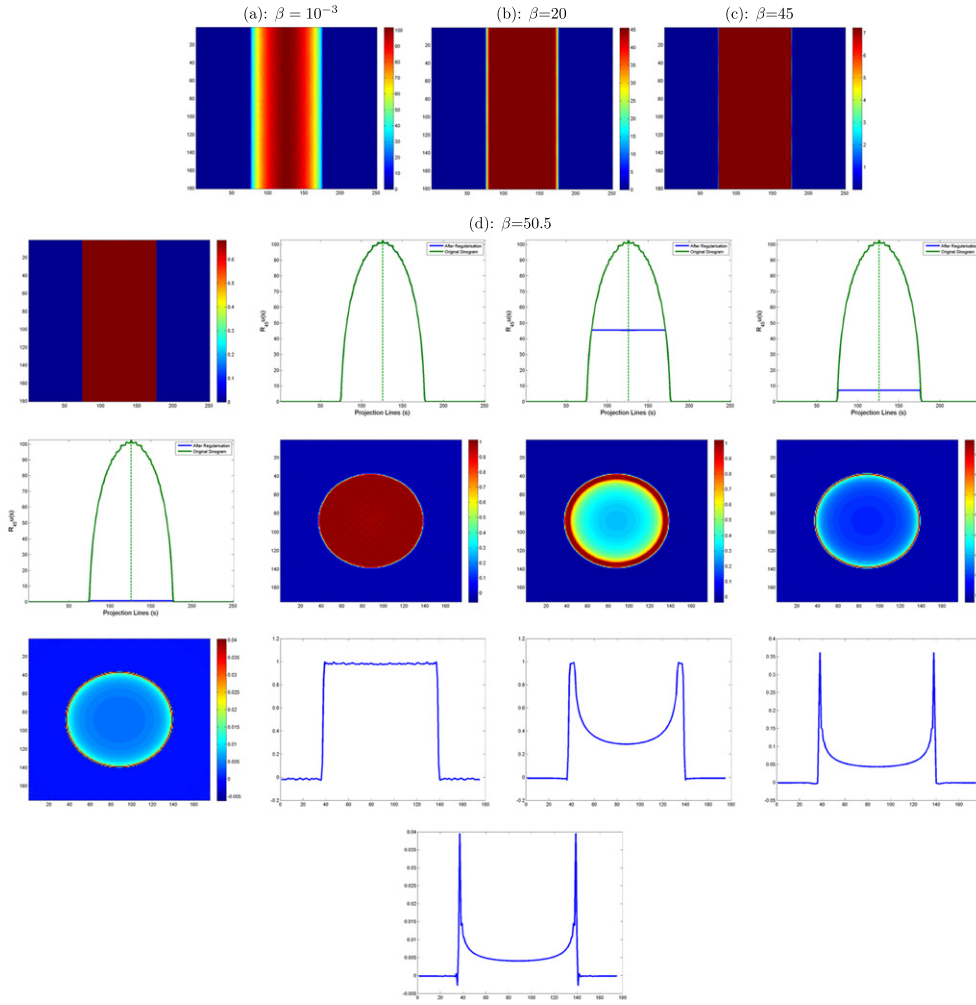**Figure 9.** Real data: best TV regularized reconstructions for noisy slice in figure 8(b).

Considering the reconstruction method (2.1) for $\alpha = 0$ results in the following weighted total variation denoising problem for the sinogram $g$

$$\arg\min_{v \geqslant 0 \text{ a.e}} \beta \parallel \nabla v \parallel_1 + \sum_{k,l} \frac{(g-v)^2}{g}, \tag{4.2}$$

where $\parallel \cdot \parallel_1$ is the discrete $l^1$ norm as defined before. Similar to before, we solve (4.2) by a Split Bregman technique, introducing two more variables $w = \nabla v$ and $\tilde{v} = v$. Then, starting with initial conditions $b_1^0 \in \mathbb{R}^{2k \times l}$ and $b_2^0 \in \mathbb{R}^{k \times l}$, we iteratively solve for $k = 1, 2, \ldots$

$$v^{k+1} = \arg\min_v \frac{\lambda_1}{2} \left\| b_1^k + \nabla v - w^k \right\|_2^2 + \frac{\lambda_2}{2} \left\| b_2^k + v - \tilde{v}^k \right\|_2^2 \tag{4.3}$$

$$\tilde{v}^{k+1} = \arg\min_{\tilde{v} \geqslant 0} \frac{1}{2} \int \frac{\left( g - \tilde{v} \right)^2}{g} + \frac{\lambda_2}{2} \left\| b_2^k + v^{k+1} - \tilde{v} \right\|_2^2 \tag{4.4}$$

**Figure 10.** Sinogram regularization with different values of $\beta$ (first row) and the corresponding filtered backprojected images (third row). The second row represents a 45° comparison of the original sinogram and the sinogram after regularization. The highest value of the sinogram is 102.8. The fourth row represents the middle line profiles of the reconstructed images in the third row.

$$w^{k+1} = \frac{\arg\min}{w} \beta \, \| w \|_1 + \frac{\lambda_1}{2} \, \left\| b_1^k + \nabla v^{k+1} - w \right\|_2^2 \tag{4.5}$$

$$b_1^{k+1} = b_1^k + \nabla w^{k+1} - v^{k+1} \tag{4.6}$$

$$b_2^{k+1} = b_2^k + v^{k+1} - \tilde{v}^{k+1}. \tag{4.7}$$

Note that, as before, in the solution of (3.19) a simple backprojection of the sinogram is used and we set $\lambda_1 = \lambda_2 = 1$. Moreover, since we do not apply any positivity constraint on the image as it is done in the full algorithm used in section 4.1, we might observe small negative values in the reconstructed images presented in the following.

**Table 3.** Comparison of analytic and numerical computations of sinogram regularization for three test images of characteristic functions of circles with radii $r = 15.5$, $30.5$ and $50.5$. The parameters $\delta^{an}$ and $\delta^{num}$ denote the analytic and numerical $\delta$, respectively, in the expression of the regularized solution in (2.30). Compare also figure 10 for regularized reconstructions for the circle with radius $r = 50.5$.

| $r = 15.5$ | $\beta$ | $10^{-3}$ | 0.1 | 1 | 5 | 10 | 15 | 15.5 |
|---|---|---|---|---|---|---|---|---|
| | $\delta^{an}$ | 30.94 | 29.88 | 25.84 | 16.09 | 7.59 | 0.64 | 0.084 |
| | $\delta^{num}$ | 31.32 | 29.76 | 25.71 | 15.96 | 7.37 | 0.67 | 0.37 |
| $r = 30.5$ | $\beta$ | $10^{-3}$ | 1 | 10 | 15 | 20 | 25 | 30.5 |
| | $\delta^{an}$ | 60.93 | 59.6 | 31.35 | 22.37 | 14.46 | 7.27 | 0.09 |
| | $\delta^{num}$ | 61.98 | 54.58 | 31.42 | 22.47 | 14.55 | 7.34 | 0.65 |
| $r = 50.5$ | $\beta$ | $10^{-3}$ | 1 | 10 | 20 | 30 | 45 | 50.5 |
| | $\delta^{an}$ | 100.92 | 93.33 | 65.74 | 45.46 | 28.71 | 7.16 | 0.12 |
| | $\delta^{num}$ | 101.83 | 93.26 | 65.75 | 45.41 | 28.82 | 7.24 | 0.68 |

First, we consider image functions with radial symmetry such as in section 2.5 equation (2.30). Figure 10 shows the numerically computed regularized sinograms and corresponding images for an original image of a disc with radius $r = 50.5$. Here we have used MATLAB's built-in function *iRadon* with a *Ram-Lak* filter and *spline* interpolation to compute the FBP of the regularized sinogram. Moreover, table 3, shows the correspondence of the numerical solution with the analytic solution in section 2.5 for three discs of radii $r = 15.5$, $30.5$ and $50.5$. Here, $\delta^{an}$ and $\delta^{num}$ denote the analytic and numerical $\delta$, respectively, in the expression of the regularized solution in (2.30). As predicted from the computations in section 2.5, we see that with increasing regularization parameter $\beta$ the regularized image more and more emphasizes the boundary of the disc.

Going beyond radial symmetry we consider three additional examples where the sinogram depends on the angle $\theta$. First, we simply consider the image that we used in the previous section in figure 5 without adding additional noise to its sinogram. The effect of $\beta$ regularization in this case is presented in figure 11. We see that as we increase $\beta$ we loose details in the image, starting again from the inner structure of the discs, while enhancing the boundaries of the objects. Here, the connection of the choice of $\beta$ with the radius of every circle is clearly visible. More precisely, for $\beta < r_2$ the boundary of the smaller circle is enhanced and for $r_2 < \beta < r_1$ the small circle is lost and the boundary of the larger circle is enhanced.

In figure 12, we present two more test images. The first one is an image of two rings with the same outer radius but with different annulus regions, compare figure 12(a). A similar scale-space analysis as for the previous examples is carried out in figure 13. Additionally to the enhancement of the outer boundaries of the two rings we see that for increasing $\beta$ regularization the reconstructed image approaches the convex hull of the two rings. This is even more apparent for the last example of a star-shaped object in figure 12(c). See figure 14, in particular.

The conclusion of this section is the motivation for the next section at the same time. Analysing the effect of total variation regularization on the sinogram by considering its scale space and its effect on the reconstructed image we have seen in figures 10–14 the potential use of this method for the enhancement and detection of object boundaries. As we will see in
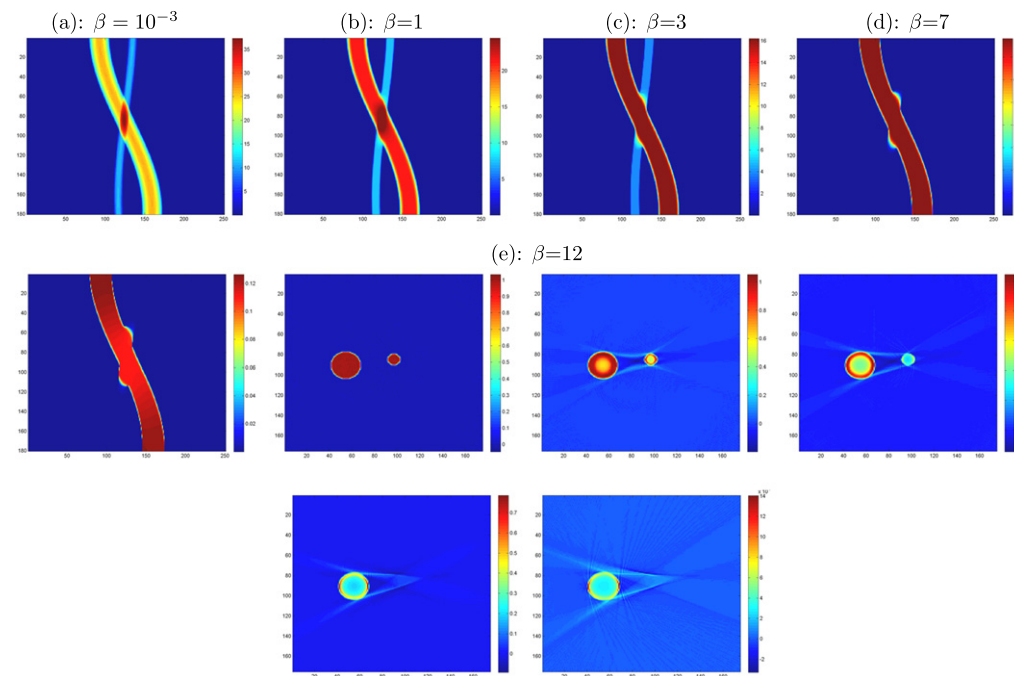
**Figure 11.** Sinogram regularization with different values of $\beta$ and the corresponding filtered backprojected images using MATLAB's *iRadon* built-in function. The radii for the discs are $r_1 = 13$ and $r_2 = 5.5$.

(a): 2 rings



(b): Sinogram



(c): Star
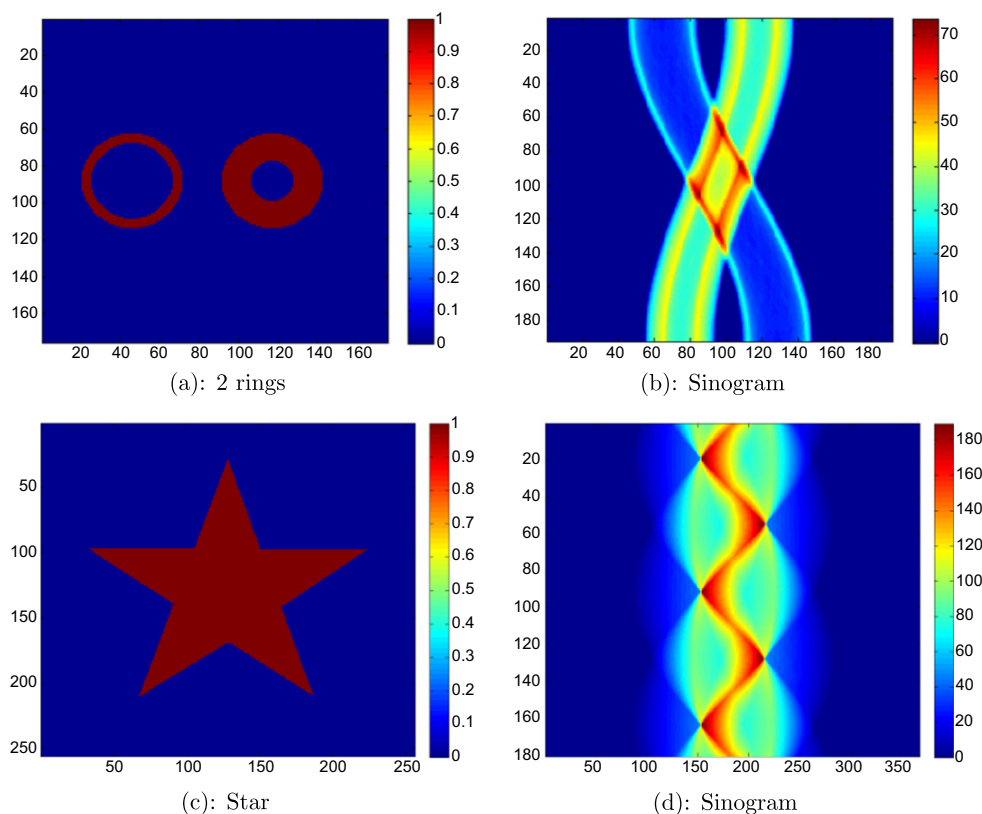


(d): Sinogram

**Figure 12.** Two rings with different annulus regions and its sinogram ((a) and (b)), star-shaped image of five points and its sinogram ((c) and (d)).

the next section, this effect can be exploited for enhancing thin structures in images obtained from Radon measurements.

### 4.3. Thin structure reconstruction

In what follows, we discuss how total variation regularization of the sinogram can improve the quality of the reconstruction in comparison with pure total variation regularization of the image in the presence of *thin* structures in the image. Our first example is a thin rectangular frame in figure 15. Similarly as in section 4.1, we start by finding an optimal value of $\alpha$ with $\beta = 0$, in terms of SNR. Then, we select a range of $\alpha$ values close to this optimal one and we allow strictly positive values for $\beta$. The noise that is added on the sinogram, is generated by MATLAB's *imnoise* routine, with a $10^{12}$ scaling factor, see the beginning of section 4 for more explanation. The test image that is shown in figure 15 has 50 pixels width and 100 pixels length and the rectangular frame has a width of 2 pixels. In figure 16, we first present some of the results obtained with pure total variation regularization on the image, that is when $\beta = 0$. As we increase the $\alpha$ parameter, we observe that the best SNR corresponds to $\alpha = 5$ with SNR = 19.9764.

(a): $\beta=0.001$　　　　(b): $\beta=1$　　　　(c): $\beta=10$

(d): $\beta=25.5$
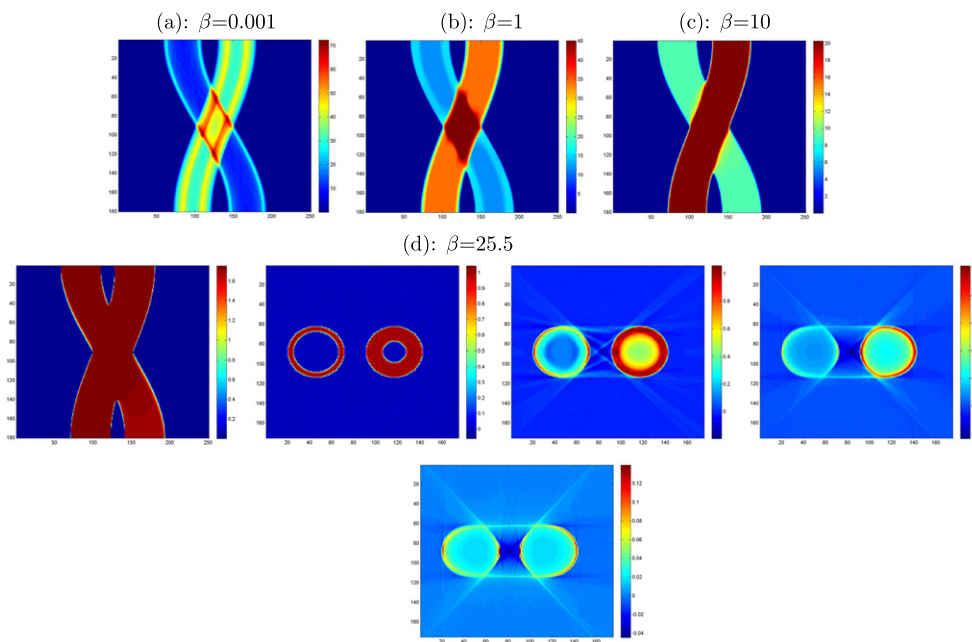


**Figure 13.** Two rings with different annulus regions: the outer radius for both rings is r = 25.5 and the inner radii are $r_1$ = 21 and $r_2$ = 11. For figures (a)–(d), we present the sinogram regularization for increasing values of $\beta$ with the corresponding filtered backprojected using MATLAB's *iRadon* built-in function.

(a): $\beta=0.001$　　　(b): $\beta=0.1$　　　(c): $\beta=1$　　　(d): $\beta=10$

(e): $\beta=50$
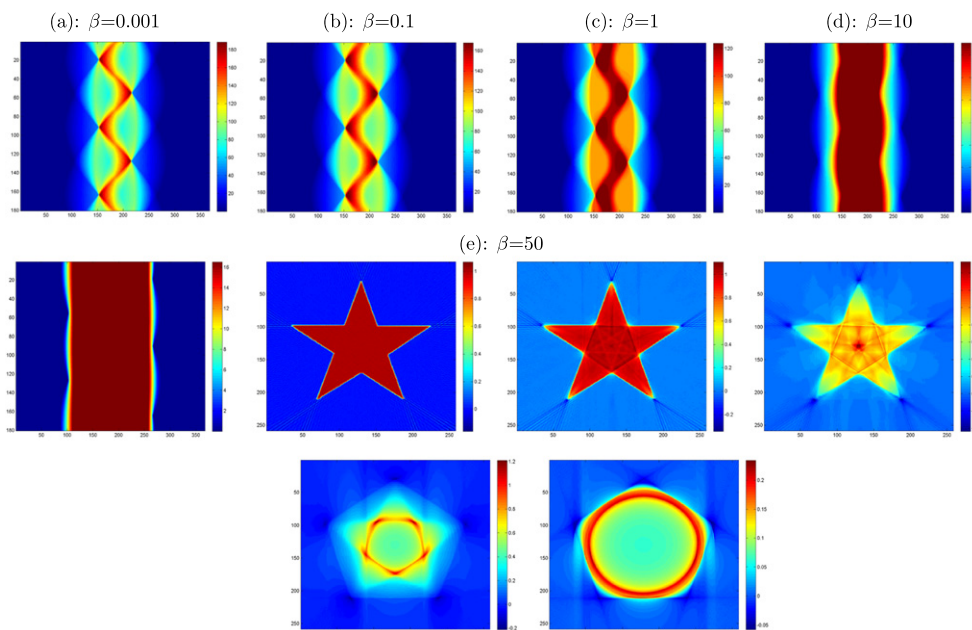


**Figure 14.** Star-shaped image of five corners: in figures (a)–(d), we present the sinogram regularization for increasing values of $\beta$ with the corresponding filtered backprojected image using MATLAB's built-in function *iRadon*.

(a): Thin Rectangle



(b): Noiseless Sinogram



(c): Low noise: SNR=14.9146
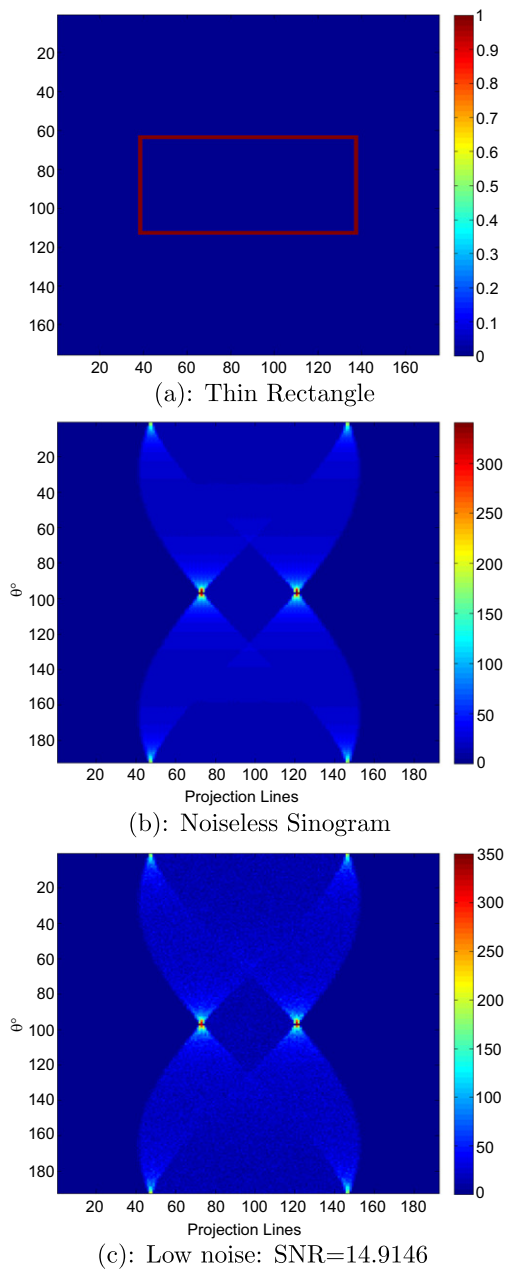
**Figure 15.** A thin rectangle of 50 pixels width and 100 pixels length with 2 pixels length on the boundaries. The corresponding noiseless and noisy sinograms with $10^{12}$ scaling factor in *imnoise*.

That is because for small values of $\alpha$ we observe that the large-scale structure of the object is still intact, with the cost that noise is still present in the reconstructed image, see figures 16(a)–(c). However, with higher values of $\alpha$ noise is further eliminated but at the
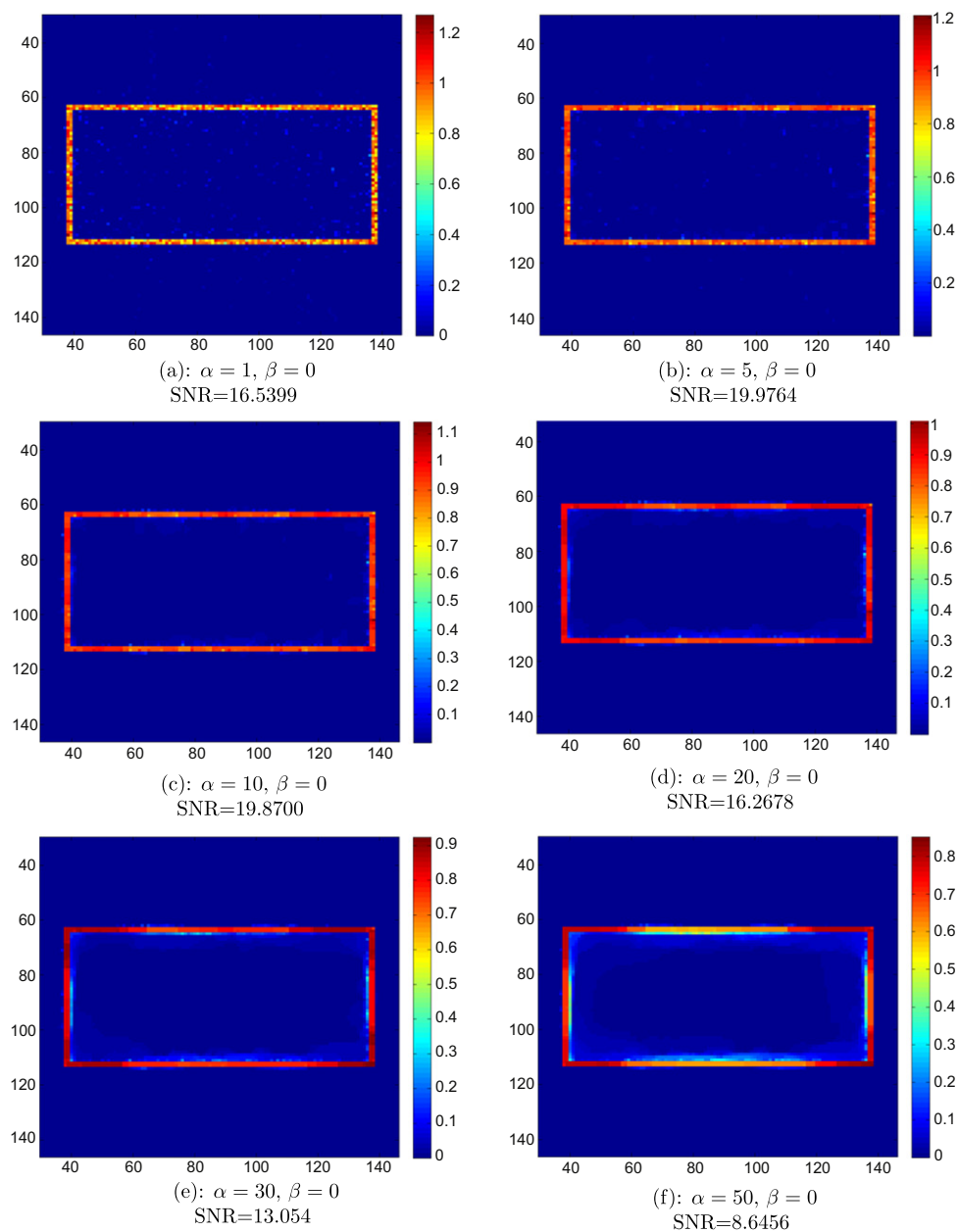
**Figure 16.** Thin rectangle: reconstruction without total variation regularization on the sinogram and different parameters of $\alpha$.

expense of a significant loss of contrast and some unpleasant artifacts along the boundaries of the frame, see figures 16(d)–(f).

If we switch on total variation regularization on the sinogram, that is taking $\beta > 0$, we obtain results which are greatly improved both in terms of the SNR of the reconstructed images but also—visually—in terms of finding the right balance of eliminating the noise and

(a): $\alpha = 7$, $\beta = 0$
SNR=20.4471

(b): $\alpha = 2$, $\beta = 0.05$
SNR=24.5981
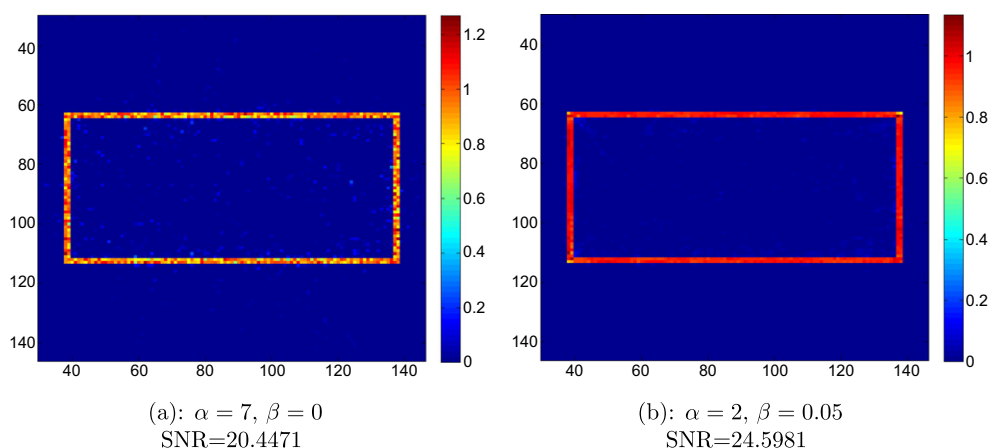
**Figure 17.** Thin rectangle: best reconstructions with and without total variation regularization on the sinogram as reported in table 4.

**Table 4.** Thin rectangle: SNR with $\beta \geqslant 0$.

|   |   | $\beta$ | | | | |
|---|---|---|---|---|---|---|
|   |   | 0 | 0.005 | 0.01 | 0.05 | 0.1 |
| $\alpha$ | 2 | 17.6798 | 18.0078 | 19.7238 | **24.5981** | 24.2978 |
|   | 3 | 18.6444 | 18.9855 | 20.6460 | 23.9028 | 24.2647 |
|   | 4 | 19.4269 | 19.7539 | 21.5305 | 23.9178 | 23.2860 |
|   | **5** | **19.9764** | 20.2979 | 21.7962 | 23.6466 | 22.8525 |
|   | 6 | 20.2583 | 20.5771 | 21.9057 | 23.2213 | 22.3440 |
|   | **7** | **20.4471** | 20.8665 | 21.8372 | 22.7554 | 21.8147 |
|   | 8 | 20.3511 | 20.3276 | 20.9859 | 22.2391 | 21.2477 |

accurately preserving the thin structures, see table 4 and figure 17. This observation is confirmed by a second example of an image of two thin straight lines which cross, compare figure 18. The width of the thin lines is 3 pixels. The length of the horizontal line is 121 pixels and of the vertical line is 100 pixels. The noise, added on the sinogram, is generated with the same scaling factor of $10^{12}$ as before. Again, we observe that for positive values of $\beta$, we obtain much better reconstructions with almost all noise eliminated while keeping the boundaries of the thin structures intact, see figure 19.

We also apply our method to a more realistic PET phantom for visualizing activity of the human heart. The XCAT phantom is a 3D phantom. For our purpose we used one z-slice through the centre of the phantom which represents a transverse plane view of the human body, see figure 20. In particular, we can see the activity of the heart through the myocardium (the muscle surrounding the heart) in red. We focus on regions where thin structures are observed, see figures 21(a)-(b) and add the usual level of Poisson noise to their corresponding sinograms, see figures 21(c)-(d). In figures 22(a)–(d) we present our best reconstructions for these two different data-regions in terms of the SNR values for both cases of with and without sinogram regularization. It is obvious that the best reconstructions are achieved when there is no regularization on the sinogram. That is because for increasing
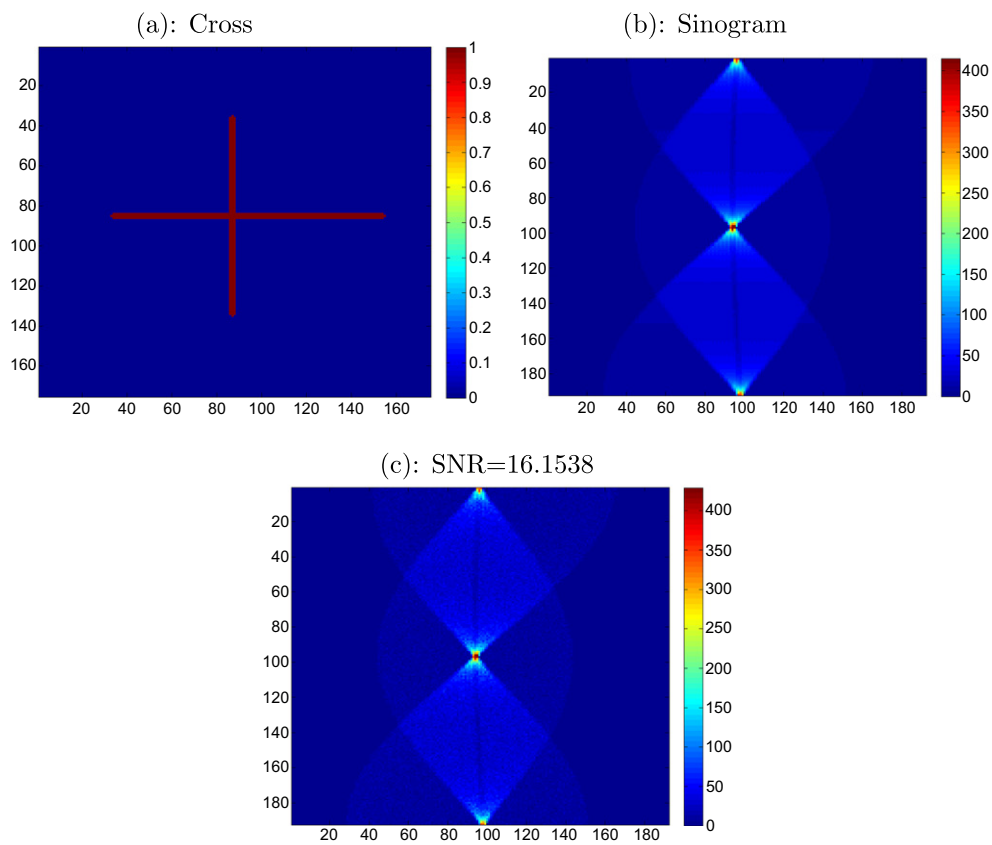
**Figure 18.** Test image of two thin crossing lines and its noiseless and noisy sinograms, respectively.
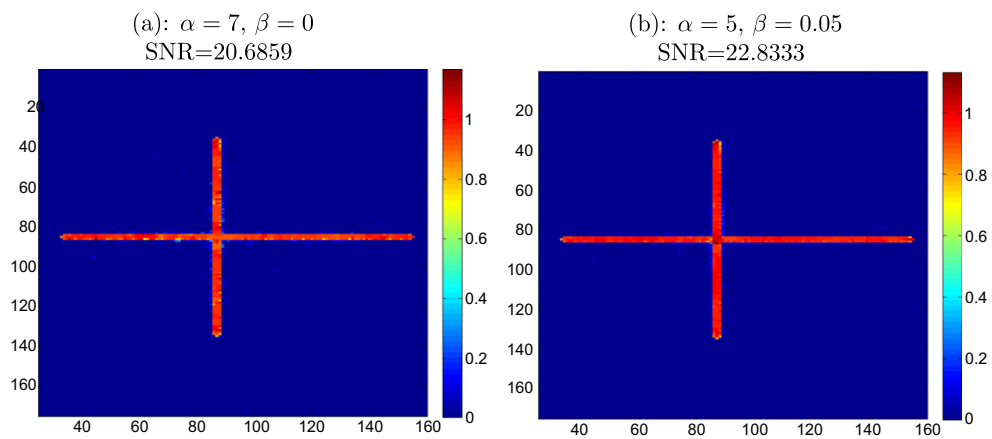


**Figure 19.** Reconstruction for the noisy sinogram in figure 18 that correspond to the best SNR for both cases of $\beta$.
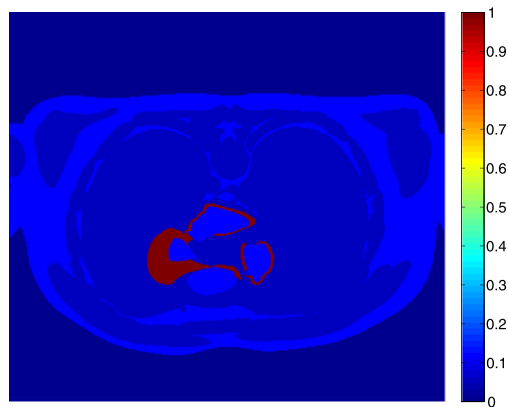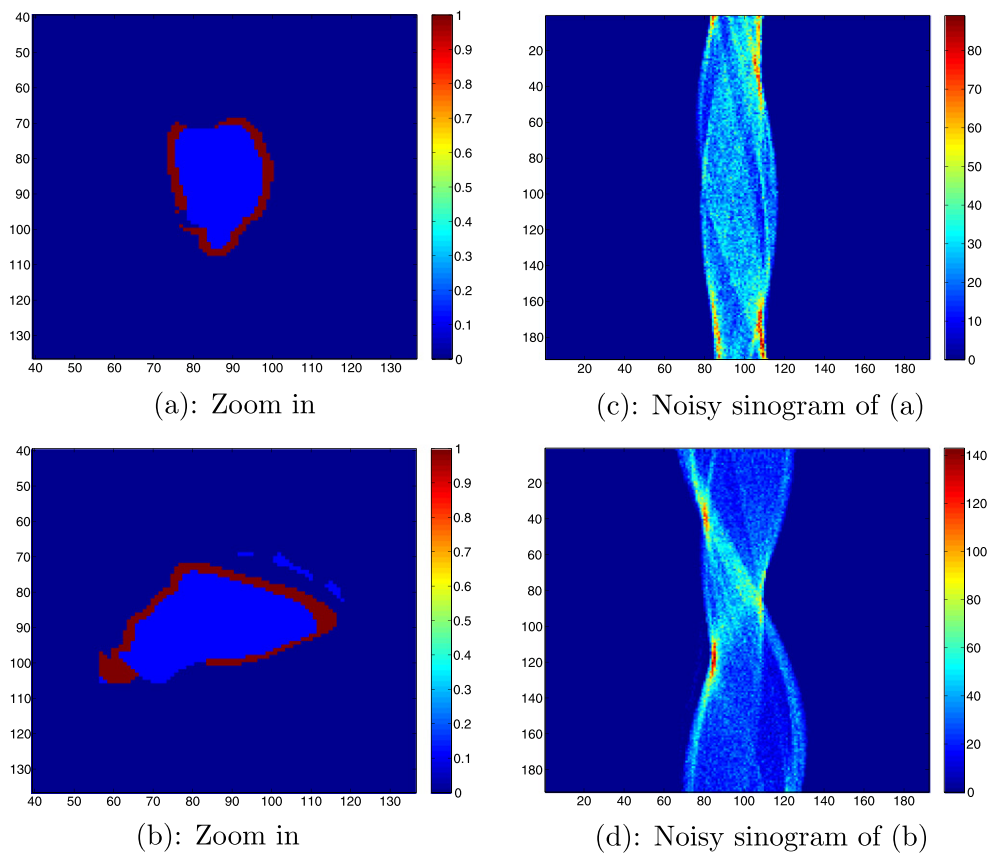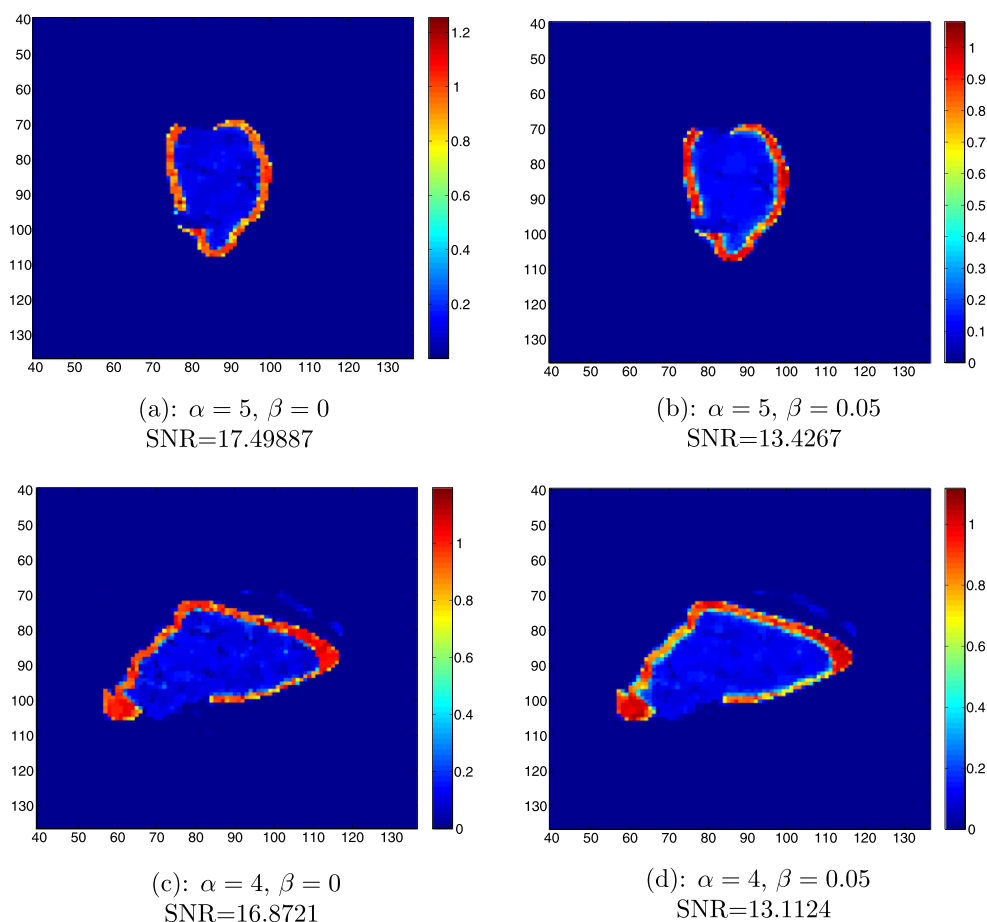
**Figure 20.** XCAT phantom.



(a): Zoom in

(c): Noisy sinogram of (a)

(b): Zoom in

(d): Noisy sinogram of (b)

**Figure 21.** Selected regions of the XCAT phantom with the corresponding noisy sinograms.

values of $\beta$ a smoothing on the originally blocky boundaries is enforced and hence the SNR value is reduced. Indeed, as we show in the following experiments this is only true if the
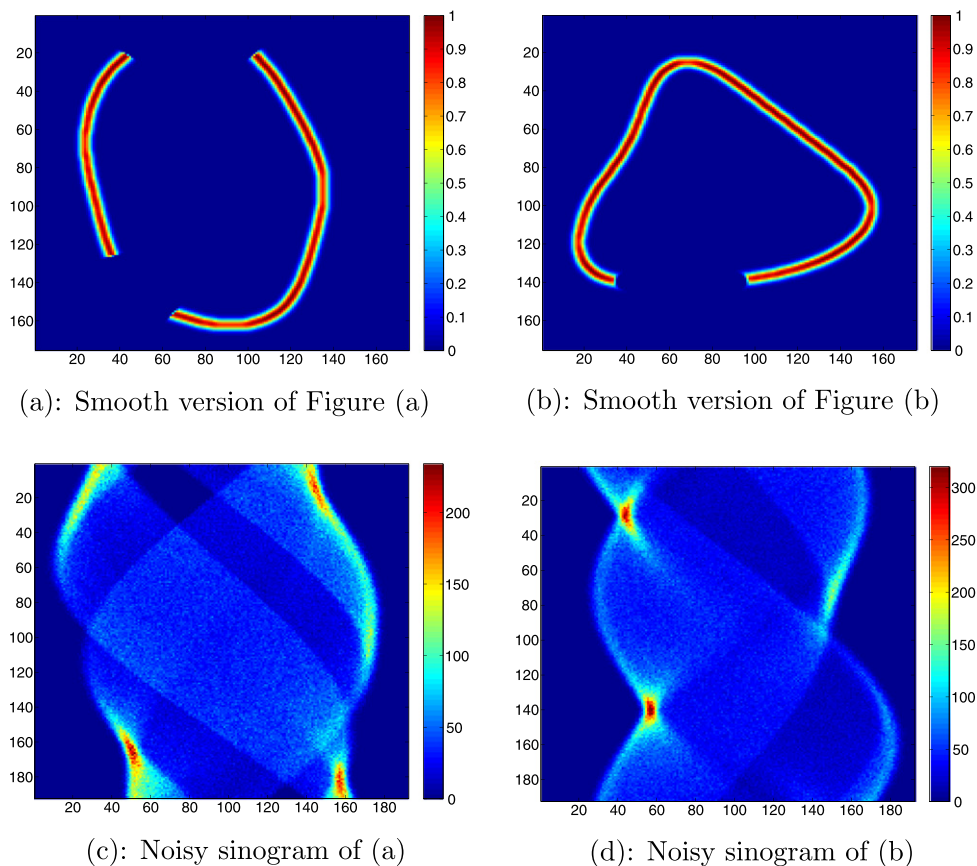
**Figure 22.** Reconstructions with and without total variation regularization on the details of the XCAT sinogram in figure 21.

initial data that we start our experiments with is of low resolution and the thin structures have *blocky* instead of smooth boundaries. If we change our experiment to the consideration of a high resolution version of the XCAT phantom with thin structures as in figures 21(a)–(b) but with medically more realistic smooth boundaries, the positive effect of the TV sinogram regularization can be observed. As it is expected, regularizing only on the image space creates a rather unpleasant staircasing effect along the boundaries which is clearly eliminated when we combine the regularization on both spaces, see figure 24. Indeed, a significant increase of the SNR when turning on the TV regularization on the sinogram ($\beta > 0$) can be observed.

## 5. Conclusion

We present a combined approach of total variation regularization of both the image and the sinogram for PET reconstruction. We prove existence, uniqueness and stability results for our proposed model with an additional error analysis through Bregman distance. Our

(a): Smooth version of Figure (a)

(b): Smooth version of Figure (b)

(c): Noisy sinogram of (a)
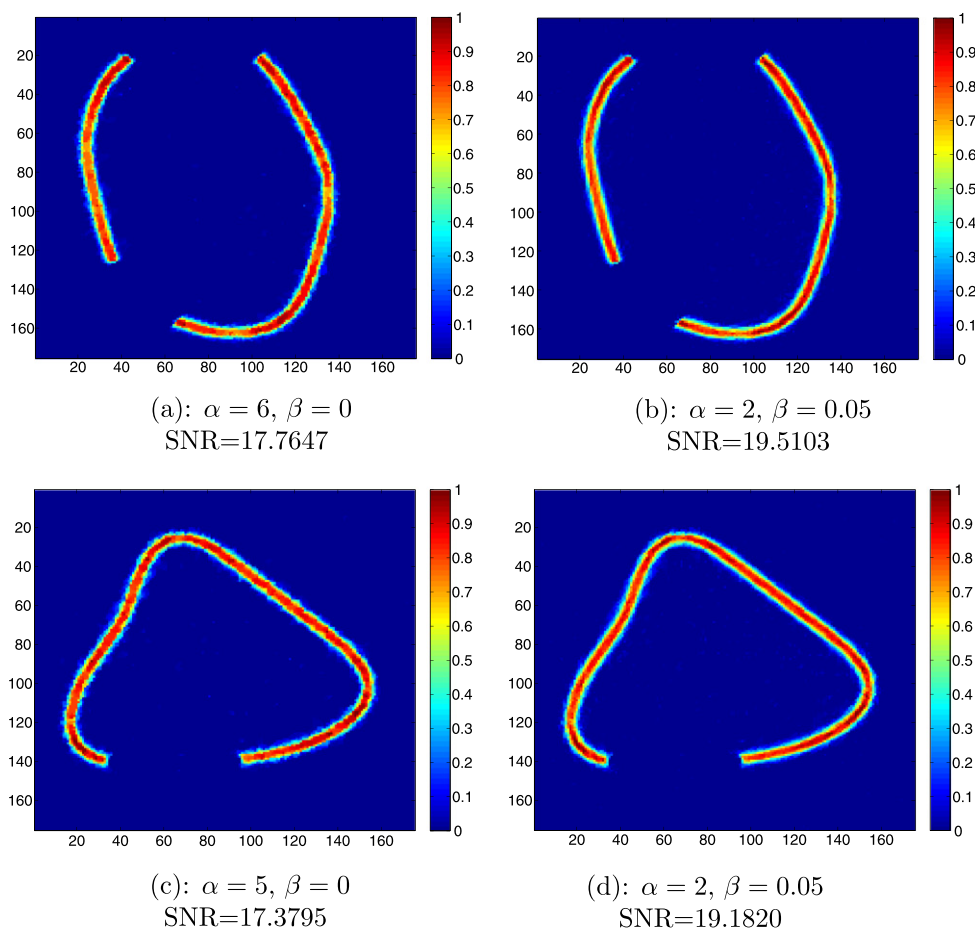
(d): Noisy sinogram of (b)

**Figure 23.** High resolution XCAT: smooth versions of figures 21(a)–(b) and their noisy sinograms.

explicit reconstruction of total variation regularization, directly on the sinogram space, provides us with a new insight on how PET reconstruction could be improved and in which cases.

We compute an optimal solution of the weighted-ROF model for a sinogram of disc in $R^2$ and find analytically the corresponding solution on the image space via the Radon transform. The weighted $L^2$ fidelity behaves as an approximation of the Poisson noise model given by the Kullback–Leibler divergence and allows us to find a crucial relation between the regularizing parameter $\beta$ and the support of our object. This connection could be verified numerically when appropriate values of $\beta$ are chosen to be close to the radius r and tend to approximate the boundaries or the convex hull of the reconstructed object. Hence, a combined penalization on both the image and the sinogram space leads us to an enhancement and detection of object boundaries, specifically for images where *thin structures* are present.

In real PET data thin structures will only make up parts of the image which will in general consist of small and larger scale objects as well as background. Our experiments for the cropped thin structures of the XCAT phantom in figure 20 suggest TV regularization on a targeted local Radon transform instead of the full Radon transform that allows to increase the regularization on the sinogram in regions with thin structures.

(a): $\alpha = 6$, $\beta = 0$
SNR=17.7647

(b): $\alpha = 2$, $\beta = 0.05$
SNR=19.5103

(c): $\alpha = 5$, $\beta = 0$
SNR=17.3795

(d): $\alpha = 2$, $\beta = 0.05$
SNR=19.1820

**Figure 24.** Reconstructions for the structures in figure 23 with and without total variation regularization on the sinogram. Smoothing along the boundaries is achieved when sinogram regularization is active, resulting in a significant improvement of the SNR.

## Acknowledgements

## References

[1]  Acar R and Vogel C R 1994 *Inverse Problems* **10** 1217–29
[2]  Ambrosio L, Fusco N and Pallara D 2000 *Functions of Bounded Variation and Free Discontinuity Problems* vol 254 (Oxford: Clarendon)

[3] Barbano P E, Fokas A and Schönlieb C B 2011 *Proc. 9th Int. Conf. on Sampling Theory and Applications (SampTA) (Singapore, 2011)* pp 1–4

[4] Bardsley J M 2010 *Inverse Problems Imaging* **4** 11–17

[5] Bardsley J M, Calvetti D and Somersalo E 2010 *Inverse Problems* **26** 035010

[6] Benning M and Burger M 2011 Error estimates for general fidelities *Electron. Trans. Numer. Anal.* **38** 44–68

[7] Benning M and Burger M 2014 Ground states and singular vectors of convex variational regularization methods *Methods Appl. Anal.* **20** 295–334

[8] Bergounioux M and Trélat E 2010 A variational method using fractional order Hilbert spaces for tomographic reconstruction of blurred and noised binary images *J. Funct. Anal.* **259** 2296–332

[9] Bregman L 1967 The relaxation of finding the common points of convex sets and its application to the solution of problems in convex programming *USSR Comput. Math. Math. Phys.* **7** 200–17

[10] Sawatzky A, Brune C, Kösters T, Wübbeling F and Burger M 2013 EM-TV methods for inverse problems with Poisson noise *Level Set and PDF Based Reconstruction Methods (Imaging Lecture Notes in Mathematics)* ed M Burger *et al* (Switzerland: Springer) pp 71–142

[11] Brune C, Sawatzky A and Burger M 2011 Primal and dual Bregman methods with application to optical nanoscopy *Int. J. Comput. Vis.* **92** 211–29

[12] Burger M and Osher S 2007 Convergence rates of convex variational regularization *Inst. Phys. Publ.* **27** 257–63

[13] Caselles V, Chambolle A and Novaga M 2007 The discontinuity set of solutions of the TV denoising problem and some extensions *Multisc. Modelling Simul.* **6** 879–94

[14] Chambolle A 2004 An algorithm for total variation minimisation and applications *J. Math. Imaging Vis.* **20** 89–97

[15] Chan T and Shen J 2005 *Image Processing and Image Analysis, Variational, PDE, Wavelet and Stochastic Methods* (Philadelphia: SIAM)

[16] Ekeland I and Témam R 1999 *Convex Analysis and Variational Problems* (Philadelphia: SIAM)

[17] Esser E, Zhang X and Chan T 2010 A general framework for a class of first order primal-dual algorithms for convex optimization in imaging science *SIAM J. Imaging Sci.* **3** 1015–46

[18] Getreuer P 2012 Rudin–Osher–Fatemi total variation denoising using split Bregman *Image Processing Online* **2** 74–95

[19] Goldstein T and Osher S 2009 The split Bregman algorithm method for l1 regularized problems *SIAM J. Imaging Sci.* **2** 323–43

[20] Hertle A 1983 Continuity of the Radon transform and its inverse on Euclidean space *Math. Z.* **184** 165–92

[21] Le T, Chartrand R and Asaki T J 2007 A variational approach to reconstructing images corrupted by poisson noise *J. Math Imaging Vis.* **27** 257–63

[22] Marinakis V, Fokas A S and Iserles A 2006 Reconstruction algorithm for single photon emission computed tomography and its numerical implementation *J. R. Soc. Interface* **6** 45–54

[23] Markoe A 2006 *Analytic Tomography* (Cambridge: Cambridge University Press)

[24] Natterer F 2001 The Mathematics of computerized tomography *Applied Mathematics* (Philadelphia: SIAM)

[25] Osher S, Burger M, Goldfarb D, Xu J and Yin W 2005 An iterative regularization method for total variation-based image restoration *Multisc. Modelling Simul.* **4** 460–89

[26] Poularikas A 2010 *Transforms and Application Handbook* 3rd edn (Boca Raton, FL: CRC Press)

[27] Prince J L and Willsky A S 1990 A geometrical projection-space reconstruction algorithm *Linear Algebr. Appl.* **130** 151–91

[28] Rudin L I, Osher S and Fatemi E 1992 Nonlinear total variation based noise removal algorithms *Physica D: Nonlinear Phenom.* **60** 259–68

[29] Sawatzky A 2011 Non local total variation in medical imaging *PhD Thesis* Wilhelms-Universität, Münster

[30] Sawatzky A, Brune C, Müller J and Burger M 2009 Total variation processing of images with poisson statistics *Computer Analysis of Images and Patterns* (Berlin: Springer) pp 533–40

[31] Sawatzky A, Brune C, Wübbeling F, Kosters T, Schäfers K and Burger M 2008 Accurate EM-TV algorithm in PET with low SNR *2008. NSS '08. IEEE Nucl. Sci. Symp. Conf. Rec.* pp 5133–7

[32] Setzer S 2009 Split Bregman algorithm, Douglas–Rachford splitting and frame shrinkage *Scale Space and Variational Methods in Computer Vision* (Berlin: Springer) pp 464–76

[33] Setzer S 2011 Operator splittings, Bregman methods and frame shrinkage in image processing *Int. J. Comput.Vis.* **92** 265–80

[34] Thirion J P 1991 A geometric alternative to computed tomography *Technical report* RR-1463 (LeChesnay, France: INRIA)
[35] Vese L 2001 A study in the BV Space of a Denoising-Deblurring Variational problem *Appl. Math. Optim.* **44** 131–61
[36] Wernick M N and Aarsvold J N 2004 *Emission Tomography—The Fundamentals of PET and SPECT* (Amsterdam: Elsevier)
[37] Willett R M, Harmany Z T and Marcia R F 2010 Poisson image reconstruction with total variation regularization *17th IEEE Int. Conf. on Image Processing (ICIP) 2010* pp 4177–80